



Contents lists available at ScienceDirect

Journal of Great Lakes Research

journal homepage: [www.elsevier.com/locate/ijglr](http://www.elsevier.com/locate/ijglr)

## Sensitivity of remotely sensed pigment concentration via Mixture Density Networks (MDNs) to uncertainties from atmospheric correction

Kiana Zolfaghari <sup>a,\*</sup>, Nima Pahlevan <sup>b,c</sup>, Stefan G.H. Simis <sup>d</sup>, Ryan E. O'Shea <sup>b,c</sup>, Claude R. Duguay <sup>a,e</sup>

<sup>a</sup> Department of Geography and Environmental Management, University of Waterloo, Waterloo, ON N2L 3G1, Canada

<sup>b</sup> NASA Goddard Space Flight Center, Greenbelt, MD 20771, USA

<sup>c</sup> Science Systems and Applications Inc., Lanham, MD 20706, USA

<sup>d</sup> Plymouth Marine Laboratory, Plymouth PL1 3DH, UK

<sup>e</sup> H2O Geomatics Inc., Waterloo, ON N2L 1S7, Canada

### ARTICLE INFO

#### Article history:

Received 6 July 2022

Accepted 12 December 2022

Available online xxxx

Communicated by A. Vodacek

#### Keywords:

Sentinel-3

OLCI

POLYMER

iCOR

ACOLITE

MDNs

### ABSTRACT

Lake Erie, the shallowest of the five North American Laurentian Great Lakes, exhibits degraded water quality associated with recurrent phytoplankton blooms. Optical remote sensing of these optically complex inland waters is challenging due to the uncertainties stemming from atmospheric correction (AC) procedures. In this study, the accuracy of remote sensing reflectance ( $R_{rs}$ ) derived from three different AC algorithms applied to Ocean and Land Colour Instrument (OLCI) observations of western Lake Erie (WLE) is evaluated through comparison to a regional radiometric dataset. The effects of uncertainties in  $R_{rs}$  products on the retrieval of near-surface concentration of pigments, including chlorophyll-*a* (Chl<sub>a</sub>) and phycocyanin (PC), from Mixture Density Networks (MDNs) are subsequently investigated. Results show that iCOR contained the fewest number of processed (unflagged) days per pixel, compared to ACOLITE and POLYMER, for parts of the lake. Limiting results to the matchup dataset in common between the three AC algorithms shows that iCOR and ACOLITE performed closely at 665 nm, while outperforming POLYMER, with the Median Symmetric Accuracy (MdSA) of ~30 %, 28 %, and 53 %, respectively. MDN applied to iCOR- and ACOLITE-corrected data (MdSA < 37 %) outperformed MDN applied to POLYMER-corrected data in estimating Chl<sub>a</sub>. Large uncertainties in satellite-derived  $R_{rs}$  propagated to uncertainties ~100 % in PC estimates, although the model was able to recover concentrations along the 1:1 line. Despite the need for improvements in its cloud-masking scheme, we conclude that iCOR combined with MDNs produces adequate OLCI pigment products for studying and monitoring Chl<sub>a</sub> across WLE.

© 2022 Published by Elsevier B.V. on behalf of International Association for Great Lakes Research.

### Introduction

The Laurentian Great Lakes system holds approximately 20 % of the world's available surface freshwater and represents an immense economic, social, and ecological engine for the region (Siman et al., 2021). Lake Erie, the shallowest (mean depth: 19 m, maximum depth: 64 m; Fay and Herdendorf, 1984) of the five North American Great Lakes, is considered highly stressed and deteriorating due to recurring phytoplankton blooms stemming from the bioavailable phosphorus in the lake as an important contributing factor (Baker et al., 2014). Lake Erie has received major scientific and media attention in the last decade due to a resurgence of cyanobacteria harmful 'algal' blooms (CyanoHABs;

see Table 1 for a list of terms and acronyms) (Watson et al., 2016). *In situ* water quality monitoring is conducted to varying extents by federal, provincial, and municipal levels of government as well as academic institutions. However, the highly dynamic nature of HABs in space and time makes it difficult to adequately capture their occurrence when relying only on conventional sampling and analysis of discrete water samples.

Remote sensing has made frequent synoptic detection, identification, and risk assessment of HABs possible. A variety of bio-optical algorithms have been developed to estimate near-surface concentrations of chlorophyll-*a* (Chl<sub>a</sub>; the primary photosynthetic pigment in all phytoplankton) and phycocyanin (PC; an accessory light-harvesting pigment that is most commonly found in cyanobacteria) from satellite imagery. However, optical remote sensing of these pigments is challenging due to atmosphere interferences and the uncertainties stemming from the application of

\* Corresponding author.

E-mail address: [kzolfagh@uwaterloo.ca](mailto:kzolfagh@uwaterloo.ca) (K. Zolfaghari).

**Table 1**  
List of terms and acronyms.

Term/Acronym	Description
AC	Atmospheric Correction
ACOLITE	Atmospheric Correction for OLI 'lite'
C2RCC	Case 2 Regional Processor
Chla	Chlorophyll-a
CyanoHAB	Cyanobacteria Harmful Algal Bloom
DSF	Dark Spectrum Fit
HICO	Hyperspectral Imager for the Coastal Ocean
iCOR	image correction for atmospheric effect
MPH	Maximum Peak-Height
MAPE	Mean Absolute Percentage Error
MERIS	Medium Resolution Imaging Spectrometer
MDN	Mixture Density Network
MSI	MultiSpectral Instrument
OLCI	Ocean and Land Colour Instrument
OLI	Operational Land Manager
PC	Phycocyanin
POLYMER	POLYNomial-based algorithm applied to MERIS
PRISMA	PRecursore IperSpettrale della Missione Applicativa
$R_{rs}$	Remote Sensing Reflectance
SeaDAS	SeaWiFS Data Analysis System
TOA	Top-Of-Atmosphere
WLE	Western Lake Erie

corresponding atmospheric correction (AC) processors (Liu et al., 2021). There are algorithms, however, that avoid (full-blown) AC by using the top-of-atmosphere (TOA) or partially corrected TOA data for pigment retrieval methods (Gower et al., 2008; Matthews et al., 2012; Wynne et al., 2008). Such approaches have been effective in the estimation of water quality parameters from red and near-infrared wavebands for relatively turbid and productive waters.

Satellite observations have increasingly been integrated operationally into inland water algal bloom monitoring to provide public information and early warning services. Programs such as the U.S. Environmental Protection Agency (EPA) Cyanobacteria Assessment Network (CyAN) project use data from the Copernicus OLCI (Ocean and Land Colour Instrument) to make initial water quality assessments in near real-time and alert managers to potential problems and emerging threats related to cyanobacteria (Schaeffer et al., 2018). The algorithm for retrieving the cyanobacteria abundance in CyAN is based on the Cyanobacteria Index (CI; Wynne et al., 2008), a spectral shape algorithm that employs the spectral albedo at 665, 681, and 709 nm. The spectral albedo is generated by removing the Rayleigh contribution and gaseous absorption from the TOA spectral radiance. Other monitoring programs, such as EOLakeWatch, have also been developed for Lake Erie. This lake has been the focus of Environment and Climate Change Canada (ECCC) research and monitoring initiatives under the Action Plan for Clean Water due to concerns over persistent degraded water quality from recurring HABs. ECCC developed the EOLakeWatch program to deliver a suite of algal bloom indices derived using OLCI for observations from 2016 to the present and its predecessor Medium Resolution Imaging Spectrometer (MERIS) from 2002 to 2011 (Binding et al., 2021). The Chla retrieval algorithm implemented in EOLakeWatch is based on the Maximum Chlorophyll Index (MCI; Binding et al., 2021; Gower et al., 2008). MCI measures the peak of TOA spectral radiance at 708 nm, relative to a baseline interpolated between the bands either side. This algorithm is particularly favorable due to its relative insensitivity to uncertainties from the atmospheric correction (Binding et al., 2021). Matthews et al. (2012) presented a novel algorithm using MERIS Rayleigh-corrected reflectance for estimating algal biomass (Chla), cyanobacteria blooms, surface scum, and floating vegetation in coastal and inland waters. The algorithm, referred to as the maximum peak height (MPH), is a red-edge baseline-subtraction algo-

gorithm using the position and magnitude of the Chla fluorescence and particulate backscatter/absorption-related peaks in the red/NIR bands of MERIS. Similar to Cyanobacteria Index, this algorithm circumvents the error-prone aerosol removal used to derive the water-leaving reflectance and corrects only for gaseous absorption and the Rayleigh scattering (not aerosols). The baseline-subtraction approach minimizes the effect of aerosols in the atmosphere (Matthews et al., 2012).

Algorithms that estimate Chla from atmospherically corrected red and near-infrared wavebands typically have the widest range of applicability, while no single (semi)empirical algorithm can retrieve Chla across all trophic states (Liu et al., 2021; Neil et al., 2019). Therefore, to observe a range of trophic conditions, AC is still considered an essential step in the remote sensing of water quality. An ideal AC removes perturbing atmospheric effects that vary as a function of imaging geometry and regional and seasonal variability in atmospheric composition. This supports the use of physics-based algorithms for biogeochemical variable retrieval, allowing for better propagation of uncertainties when validation data are typically scarce. There exist several AC algorithms for multispectral satellites. A new coastal AC algorithm is developed by Schroeder et al. (2022) to process Sentinel-3 OLCI data. This algorithm is based on the inversion of radiative transfer (RT) simulations in a coupled atmosphere-ocean system using artificial neural networks (ANN). The evaluation analysis in this study was performed in the coastal waters of the Great Barrier Reef, Australia, and resulted in a band-averaged (412 – 708 nm) mean absolute percentage error (MAPE) of 16 % (Schroeder et al., 2022). The AC for OLI 'lite' (ACOLITE; Vanhellemont and Ruddick, 2016) processor was applied to Landsat-8 (L8) Operational Land Imager (OLI) and Sentinel-2-MultiSpectral Instrument (MSI) images over the turbid waters of the Río de la Plata estuary in (Maciel and Pedocchi, 2022). The most recent methodology in ACOLITE, the dark spectrum fit (DSF), is particularly suitable for sediment-rich waters (Pahlevan et al., 2021). The study by Renosh et al. (2020) applied several AC algorithms to MSI and OLCI data over moderately to highly turbid estuarine waters in the Gironde Estuary (France). Some of the algorithms applied to OLCI data include image correction for atmospheric effects (iCOR; de Keukelaere et al., 2018), POLYNomial-based algorithm applied to MERIS (POLYMER; Steinmetz et al., 2011), and the neural-net based algorithm Case 2 Regional processor (C2RCC; Doerffer and Schiller, 2007). Windle et al. (2022) used a regional *in situ* dataset from the Chesapeake Bay to evaluate the performance of four AC algorithms applied to OLCI data, including C2RCC, POLYMER, SeaDAS, and the standard Level-2 OLCI data (Baseline Atmospheric Correction; BAC). The statistical metrics demonstrated that C2RCC had the best performance for their dataset, particularly for longer wavelengths (>560 nm). Pahlevan et al. (2021) performed a thorough evaluation of eight AC processors for Landsat-8 and Sentinel-2 data in the Atmospheric Correction Intercomparison Exercise (ACIX-Aqua), a joint NASA – ESA activity. The largest uncertainties in the best-performing processors were associated with the blue bands (25 to 60 %). POLYMER was applied to Sentinel-2 MSI and Sentinel-3 OLCI data in Warren et al. (2021) to retrieve Chl-a and turbidity data. Finally, O'Shea et al. (2021) employed a machine learning model called Mixture Density Network (MDN; Pahlevan et al., 2020) to estimate Chla and PC from remote sensing reflectance ( $R_{rs}$ ). To reduce the sensitivity to AC, a combination of band ratios and line heights was also used in the model development. MDN was applied to hyperspectral HICO (Hyperspectral Imager for the Coastal Ocean) and PRISMA (PRecursore IperSpettrale della Missione Applicativa) data which were atmospherically corrected using the SeaWiFS Data Analysis System (SeaDAS v7.5.3; Ibrahim et al., 2018) and the Atmospheric and Topographic Correction (ATCOR v.9.3.0; Richter and Schläpfer, 2002), respectively.

Uncertainties in  $R_{rs}$  estimations are propagated to any derived water quality product, depending on the sensitivity of the retrieval algorithms (Liu et al., 2021). In this study, the application of AC algorithms to OLCI data for retrieving  $R_{rs}$  and MDN in simultaneously estimating Chla and PC from atmospherically-corrected OLCI datasets is examined for western Lake Erie (WLE). The AC algorithms selected in this study include iCOR, ACOLITE, and POLYMER processors, all of which were analyzed in Pahlevan et al., 2021. iCOR and ACOLITE were particularly identified as top performers across highly eutrophic waters. POLYMER is, on the other hand, known for its capability in dealing with sunglint pixels and has been shown to perform with varying degrees of success in different regions (Warren et al., 2019). Our objectives include: (1) the evaluation of atmospherically-corrected  $R_{rs}$  products, derived from the application of the three AC processors to OLCI, using field-measured hyper- and multi-spectral radiometric data; (2) the evaluation of MDN (O'Shea et al., 2021) based Chla and PC products estimation from the three atmospherically-corrected OLCI datasets; and (3) a comparison of the derived products (atmospherically-corrected  $R_{rs}$ , Chla and PC) using a common matchup dataset among the three AC algorithms.

## Methods and datasets

### Study area and *in situ* measurements

The selected study site, WLE, is the shallowest part of the lake (Fay and Herdendorf, 1984) with CyanoHABs recurring annually. WLE *in situ* data employed in this study were provided by the National Oceanic and Atmospheric Administration (NOAA) Great Lakes Environmental Research Laboratory (GLERL), from 2016 to 2019. Part of the WLE radiometric data were collected from the Aerosol Robotic Network (AERONET; Zibordi et al., 2009) located at 41.826° N / 83.194° W, from 2016 to 2019. Fig. 1 displays WLE and the locations of monitoring stations.

During the bloom season (June – Oct), NOAA-GLERL measures upwelling ( $L_u$ ) and sky ( $L_{sky}$ ) radiance during weekly water sampling efforts, with a Satlantic Hypergun with radiance values at 137 channels and 1 nm intervals, in the range of 348.42 – 802.4 nm. Radiance data are radiometrically calibrated, and dark-offset corrected using factory calibration files. Water leaving radiance ( $L_w$ ) is corrected for diffuse sky contamination ( $L_w = L_u - 0.028 \times L_{sky}$ ; Mobley, 1999). After calculation of down-

welling irradiance ( $E_d$ ), surface water  $R_{rs}$  was calculated as  $L_w$  divided by  $E_d$ . In addition, surface water samples (at a depth of approximately 0.75 m; Binding et al., 2012, Binding et al., 2010) are collected from the lake using Niskin bottles sampler (General Oceanic's Model 1010). Samples are then stored in the dark and transported to NOAA-GLERL to measure the Chla and PC. Details about the collection and processing of water samples, as well as the *in situ* radiometric measurements are described in Zolfaghari et al. (2021).

Following Pahlevan et al. (2021) and Spyrakos et al. (2018), Zolfaghari et al. (2021) developed a subset of Optical Water Types (OWTs). To assign each  $R_{rs}$  spectrum to one of the pre-defined OWTs, the  $R_{rs}$  values were first standardized by dividing them by the area under the curve. After standardization, the similarity of each spectrum to the associated spectrum for each OWT was calculated applying the L2 norm (Euclidean) distance. Each spectrum was then assigned to OWT with the closest distance. Fig. 2 displays the average of hyperspectral data collected by NOAA-GLERL in WLE for each. Fig. 3 shows the variability of *in situ* Chla and PC data for each OWT. OWTs 1 (N = 24) and 2 (with largest number of samples; N = 104) are the common spectra found in oligotrophic and/or coastal waters. OWTs 3 (N = 78) and 4 (N = 48) belong to lakes and coastal estuaries with increasing phytoplankton bloom densities and turbidity associated with detrital matters. OWT5 with the smallest number of samples (N = 13) represents waters high in sediment. More information about OWT extractions and their characteristics can be found in Spyrakos et al. (2018) and Zolfaghari et al. (2021).

Accurate comparison between spectral data collected from field measurements and by Sentinel-3A/B sensors requires consideration of the differences in their spectral band characteristics (i.e., central wavelength, bandwidth, and Relative Spectral Response functions -RSR-) (de Keukelaere et al., 2020). The NOAA-GLERL hyperspectral radiometric data were convolved with the relative spectral response function of OLCI to simulate their band-equivalent  $R_{rs}$  for the evaluation of AC algorithms. Fig. 4 shows a comparison between the spectral band characteristics of AERONET-OC and Sentinel-3 sensors. Therefore, the assumption of having similar spectral characteristics between *in situ*  $R_{rs}$  data and the ones collected by OLCI is valid in this study.

Radiometric data collected at the AERONET-OC station cover 8–11 bands within the 411 – 1020 nm range. Chla and PC are not included in the measurements at this station. This dataset is used for the evaluation of AC algorithms for OLCI bands within 411 –

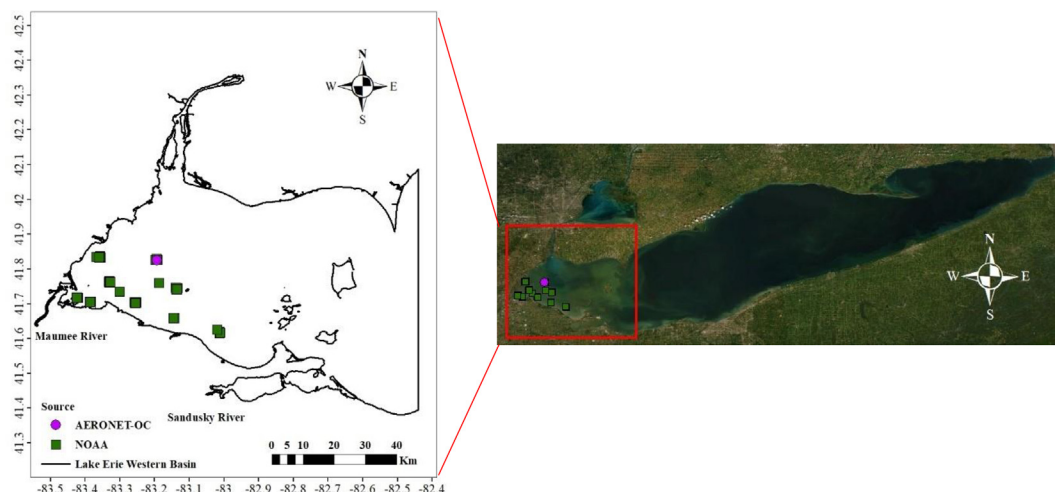


Fig. 1. Western Lake Erie (WLE) and location of the collected *in situ* data.

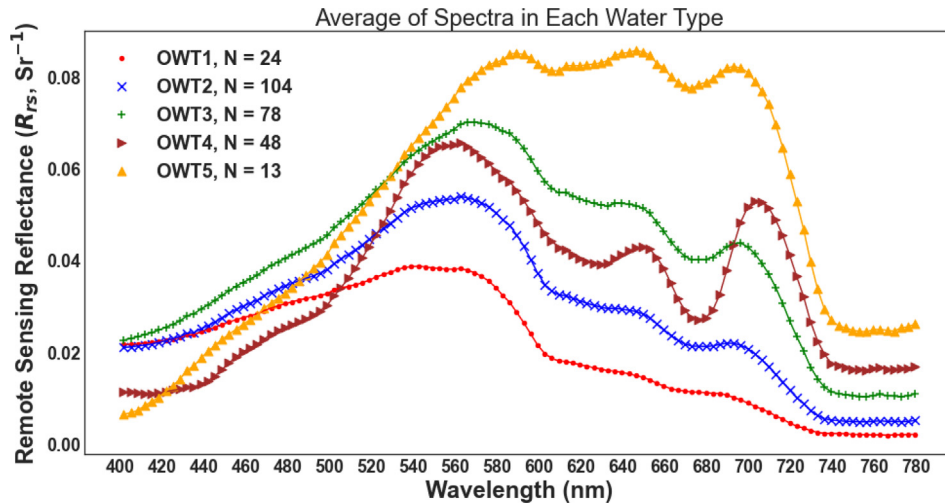


Fig. 2. Average of NOAA-GLERL hyperspectral data in each OWT, collected in June–October from 2016 to 2019. N is the number of *in situ* spectra assigned to each OWT.

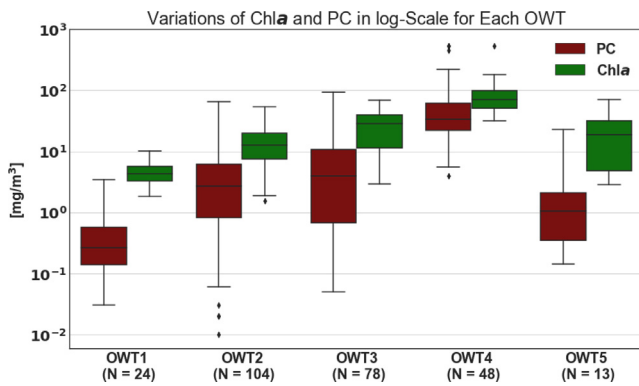


Fig. 3. Ranges of Chla and PC data collected from WLE by NOAA-GLERL (in June–October from 2016 to 2019) are displayed in log scale for each OWT in a box and whisker plot. The boxes display the median and the 25% and 75% quartiles of all data in each OWT. The whiskers are a representation of 1.5 multiplication of an interquartile range. Points are values outside this range.

709 nm (excluding the one at 675 nm). More detailed information about this station (SeaPRISM; the Sea-Viewing Wide Field-of-View Sensor (SeaWiFS) Photometer Revision for Incident Surface Mea-

surements) is available in Moore et al. (2019). Level 2.0 data (i.e., cloud-screened and quality controlled) collected at SeaPRISM station from July 2016 to September 2019 were downloaded from <https://aeronet.gsfc.nasa.gov/>. The normalized water-leaving radiance ( $L_{wn}$ ) data were converted into  $R_{rs}$  using Eq. (1) and the  $F_0$  (the *exo*-atmospheric solar irradiance,  $mW\ cm^{-2}\ \mu m^{-1}$ ) from Thuillier et al. (1998).

$$R_{rs}(\lambda) = \frac{L_{wn}(\lambda)}{F_0(\lambda)} \quad (1)$$

The OLCI band at 400 nm and the ones longer than 780 nm were excluded from the following evaluation analysis, due to inadequate radiometric coverage in the *in situ*  $R_{rs}$  data collected by NOAA-GLERL and at AERONET-OC station.

#### Atmospheric correction algorithms

The list of AC processors evaluated for  $R_{rs}$ , Chla, and PC retrieval in WLE, and their settings (processor default values) is provided in Table 2. A short description of each is summarized in the following sections.

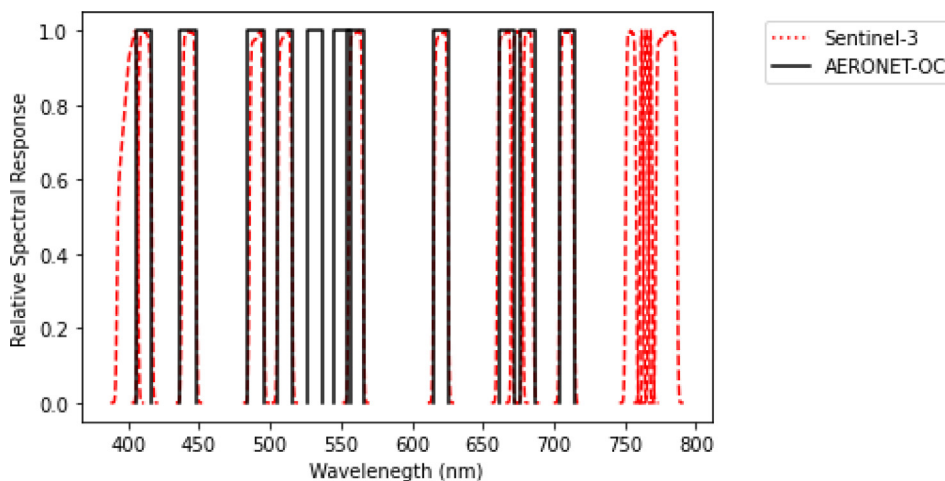


Fig. 4. Relative Spectral Response function of Sentinel-3 OLCI sensor and AERONET-OC bands plotted in dotted red and black lines, respectively. (For interpretation of the references to color in this figure legend, the reader is referred to the web version of this article.)

**Table 2**

List of AC processors applied to Sentinel-3 images in this study and their characteristics (AE: adjacency effect correction, SG: sun glint correction, CM: cloud mask).

Processor	iCOR (V7.0)	ACOLITE (V20211124.0)	POLYMER (V4.12)
<b>Principle</b>	$R_{rs}$ is retrieved from aerosol attributes removal based on land pixels within the sub(scene) (de Keukelaere et al., 2018).	$R_{rs}$ is retrieved from aerosol attributes removal based on atmospheric path reflectance computed from the dark pixel within the (sub)scene (Vanhellemont, 2019).	$R_{rs}$ is retrieved through spectral optimization of a coupled atmosphere-water system (Steinmetz et al., 2011).
<b>Feature</b>	Designed for both land and inland waters, but not oceans (Warren et al., 2019).	Designed to work best for turbid and productive waters (Pahlevan et al., 2021).	Specifically designed for water color remote sensing, and sunglint removal (Müller et al., 2015; Soppa et al., 2021).
<b>AE</b>	No	No	No
<b>SG</b>	No	No	Yes
<b>CM</b>	Yes*	Yes	Yes (Idepix)

\* However, the current research demonstrates that iCOR cloud mask is not effective.

### iCOR

iCOR is developed and maintained by the Remote Sensing group from the Vlaams Instituut voor Technologisch Onderzoek (VITO) ((de Keukelaere et al., 2018). It uses the Moderate-Resolution Atmospheric Radiance and Transmittance Model-5 (MODTRAN5) for calculation of radiative transfer model and uses Look-Up Tables (LUT) for speeding up the process (de Keukelaere et al., 2020). iCOR is a fully image-based correction approach requiring no additional user inputs. iCOR finds the land pixels within the scene and determines the aerosol optical thickness using the spectral variability of those pixels. If this fails, a default value of 0 is used for aerosol optical thickness, and only Rayleigh correction will be applied. Therefore, iCOR is a fully self-contained method which makes it ideal for batch processing and operational monitoring programs (Kravitz et al., 2020). iCOR is designed for both land and inland waters, but is not suitable for the ocean (since it requires a sufficient number and distribution of land pixels for the best results; Warren et al., 2019). Warren et al. (2019) demonstrated that iCOR errors decrease in inland waters compared to coastal waters, due to a better approximation of aerosol from the presence of more land pixels. Kravitz et al. (2020) applied iCOR on OLCI data, as well as a suite of other AC models, to retrieve Chla concentration in four inland water reservoirs in South Africa. Their results show that the application of semi-analytic Chla retrieval algorithms to *in situ*  $R_{rs}$  proved very successful for these small water targets; however, Chla results did not improve when the same retrieval algorithms were applied to iCOR processor in conjunction with an adjacency correction model. iCOR was originally developed for multispectral sensors with high spatial resolution and have now been extended to an OLCI compatible processor too.

### ACOLITE

ACOLITE is an AC processor developed by the Royal Belgian Institute of Natural Sciences (RBINS) (Vanhellemont and Ruddick, 2016). It was developed for marine waters but is also applicable to inland waters (Tóth et al., 2021). ACOLITE is an AC method that estimates water-leaving radiance by simulating contributions from molecular (Rayleigh) and particulate (aerosol) scattering using a 6SV-based look-up table (LUT) (Ilori and Knudby, 2020;

Kotchenova et al., 2008). The version of ACOLITE used in this study applies the DSF scheme, which assumes a homogenous atmosphere within the considered (sub)scene. This subscene contains pixels with near-zero water-leaving radiances in one band (Vanhellemont, 2019). ACOLITE was originally designed for Landsat (5/7/8) but has been modified and updated to process Sentinel-2 (A/B) data.

Note that the ACOLITE version applied to OLCI imagery in this manuscript (V20211124.0) corrected for gas transmittance twice (as per the ACOLITE User Manual V20221025). Additionally, the version applied to OLCI imagery in our work did not apply the European Organisation for the Exploitation of Meteorological Satellites (EUMETSAT) system vicarious calibration (SVC) gains that are applied as of ACOLITE V20221025.0. Due to these two differences, resulting OLCI  $R_{rs}$  presented in this work (using V20211124.0) will likely be biased high relative to OLCI  $R_{rs}$  produced using the most up-to-date ACOLITE code.

### POLYMER

A major issue in the AC for ocean color applications is sun glint. POLYMER, developed by HYGEOS (Lille, France), is designed to recover ocean color parameters in the whole sun glint pattern (Steinmetz et al., 2011). This correction algorithm is based on an iterative coupled ocean-atmosphere and polynomial spectral matching technique where one component describes glint (Giannini et al., 2021). A full description of the POLYMER algorithm is provided in Steinmetz et al. (2011). Several studies (Giannini et al., 2021; Pereira-Sandoval et al., 2019; Warren et al., 2019) have evaluated the performance of POLYMER on multispectral data and showed that it can outperform other existing AC methods, due to its ability to handle thin clouds and sun glint (Soppa et al., 2021). The application of POLYMER to retrieve  $R_{rs}$  from MERIS over the Baltic Sea is compared to the application of a few other AC algorithms in Qin et al. (2017). Results of this study show that POLYMER scored the highest based on a set of statistical tests (Qin et al., 2017). The research by Mograne et al. (2019) compared the performance of POLYMER applied to OLCI bands with five other AC algorithms in two bio-optical contrasted French coastal waters. Their results showed that POLYMER had the fastest processing time and scored the highest accuracy when using the common matchup dataset between all the five AC algorithms. POLYMER was originally developed to process MERIS data; however, it has been extended to process other multispectral sensor data.

In this study, OLCI images were first masked using Identification of pixel properties (IdePix; developed by Brockmann Consult) in Sentinel Application Platform (SNAP) to exclude land, cloud, ice, and snow (although the study time period is ice- and snow-free, from June to October). The internal masking routines of POLYMER were disabled. The L2 bio-optical model of POLYMER was initialized at  $10 \text{ mg m}^{-3}$  Chla and  $10 \text{ g m}^{-3}$  suspended matter (the default settings are one order of magnitude lower) and with extended bounds (0–1000 for each concentration range).

### MDN

Mixture Density Networks (MDNs) differ from traditional neural networks in that they produce a mixture model to generate estimates (Bishop, 1994). Succinctly, MDNs learn a probability distribution over the output space to learn multimodal target distributions. This multimodality is a fundamental characteristic of inverse problems, where a non-unique relationship exists between input and output features. Using the probabilities generated for each prediction, users may choose the maximum likelihood estimate (the prediction with the highest probability) or the weighted average of all predictions. The model input and output features are *in situ*  $R_{rs}$  and *in situ* Chla or PC, respectively (O'Shea et al., 2021;

Pahlevan et al., 2020b). The multimodal representation within the target space allows for enhanced predictions compared to other machine learning (ML) models. Traditional ML models like multi-layer perceptron (MLP) or other empirical Chla models, however, report a single estimate without insights into the distribution of estimates. Research by Smith et al. (2021) has shown that for a Chla retrieval task from Landsat-8/OLI observations, MDNs outperformed traditional MLPs by 20 to 30 %, an improvement attributable to the MDNs' ability to handle the multimodal nature of inverse problems. MDNs inherently learn the covariances among the output features, improving the accuracy over models intended for retrieving an individual parameter (Bishop, 1994). O'Shea et al. (2021) showed that PC can be approximated from *in situ* hyperspectral observations with a median accuracy of 44 % and a linear response for a broad range of cyanobacteria biomass. Other studies have underscored the degradations in both Chla and PC estimates from satellite observations compared to those from *in situ* radiometric spectra (O'Shea et al., 2021; Pahlevan et al., 2020a; Smith et al., 2021).

#### Performance indicators

The performance of different approaches in estimating  $R_{rs}$ , Chla, and PC from different AC algorithms was examined using both linear and log-transformed metrics. The linear metrics include MBE (mean bias error), RMSE (root mean squared error), and MAPE (mean absolute percentage error). The log-transformed metrics consist of SSPB (symmetric signed percentage bias), MdSA (median symmetric accuracy), MSA (mean symmetric accuracy), and RMSLE (root mean square log-error). The evaluation metrics are carried out using the estimated values (E) against the measured *in situ* data (M). The metrics are calculated as follows:

$$SSPB = 100 \text{sign}(z) \left( 10^{|z|} - 1 \right) [\%], \text{ where } z = \text{Median} \left( \log_{10} \left( \frac{E}{M} \right) \right) \quad (2)$$

$$MdSA = 100 \left( 10^y - 1 \right) [\%], \text{ where } y = \text{Median} \left| \log_{10} \left( \frac{E}{M} \right) \right| \quad (3)$$

$$MSA = 100 \left( 10^y - 1 \right) [\%], \text{ where } y = \text{Mean} \left| \log_{10} \left( \frac{E}{M} \right) \right| \quad (4)$$

$$RMSLE = \left[ \frac{\sum_{i=1}^N \left( \log_{10}(E_i) - \log_{10}(M_i) \right)^2}{n} \right]^{\frac{1}{2}} \quad (5)$$

$$MBE = \left[ \frac{\sum_{i=1}^N (E_i - M_i)}{n} \right] \quad (6)$$

$$RMSE = \left[ \frac{\sum_{i=1}^N (E_i - M_i)^2}{n} \right]^{\frac{1}{2}} \quad (8)$$

$$MAPE = \frac{1}{n} \sum_{i=1}^N \left| \frac{M_i - E_i}{M_i} \right| \quad (9)$$

The logarithmic metrics of SSPB, MdSA and MSA are symmetric and resistant to outliers (Morley et al., 2018). The Theil-Sen estimator slope (Theil, 1950) method is non-parametric, robust to outliers, and can produce accurate confidence intervals even when the data is not normally distributed or when it represents heteroskedasticity (Mancino et al., 2022). The Theil-Sen estimator slope with a 90 % confidence interval is produced here. MBE, RMSE, and MAPE are also included to facilitate comparisons with the pre-

viously published results. MdSA is the central metric for intercomparisons. Spectral angle mapper (SAM; Yuhas et al., 1992) is a spectral classification used in this study to calculate the similarity between the reference spectra (*in situ* data) and  $R_{rs}$  spectra produced from each AC processor.

To compare the satellite-derived and field data, differences in their spatial and temporal scales must be considered. *In situ* data are ideally collected from homogeneous areas, to minimize the effect of small-scale horizontal and temporal variations and to compensate for potential geolocation errors in the satellite data. Therefore, an average value of pixels (nominal pixel size: 300 m) within a  $3 \times 3$  window was used at each location. Only the window average values that have concurrent *in situ* data at the center pixel and have more than five neighbor pixels with valid (depending on the flags in each algorithm)  $R_{rs}$  values in the window were extracted for producing the metrics. Pixels with negative  $R_{rs}$  were also excluded from the evaluation and MDN retrievals. Although a maximum time window of three hours around the satellite overpass time for homogenous water masses is recommended (Bailey and Werdell, 2006), due to the scarcity of *in situ* measurements around satellite overpasses, a larger time window of one day (time difference between satellite and field data acquisition) was considered to increase the size of the matchup dataset.

## Results

### Evaluation

This section presents the evaluation results of OLCI atmospherically corrected products and the derived Chla and PC values for each algorithm. Evaluation metrics are shown only for bands shorter than 710 nm. The error values at wavebands longer than 710 nm were much larger than the ones for shorter bands, because the  $R_{rs}$  values are smaller in this spectral region (as plotted in Electronic Supplementary Material (ESM) Figs. S1, S3, and S5). In each processor, the size of the matchup dataset for Chla and PC evaluation is smaller than the ones for  $R_{rs}$  evaluation because of the absence of co-located Chla and PC data at the AERONET-OC station.

### iCOR

**Atmospheric correction.** A batch of 219 OLCI images processed with iCOR (iCOR4S3) had concurrent *in situ* measurements. There were 446 concurrent *in situ* measurements (i.e., matchups) of radiometric data, Chla, and PC with iCOR-corrected OLCI overpasses between 2016 and 2019 in WLE. iCOR cloud flag was used to exclude invalid pixels. 297 matchups were collected from the AERONET station with no field measurements of Chla, PC, and OLCI bands at 674, 754, and 779 nm. There were no measurements of OLCI bands at 510, 560, 620, 682, or 709 nm for the 50 matchups collected from the AERONET station.

Fig. 5 shows iCOR- $R_{rs}$  values plotted against the *in situ* measurements for selected OLCI bands. iCOR produced the  $R_{rs}$  values for all OLCI bands shorter than 780 nm except those affected by Oxygen-A absorption, i.e., at 761, 764, and 767 nm. From SSPB, iCOR derived  $R_{rs}$  is biased high below 550 nm and biased low above 550 nm (ESM Fig. S2, SSPB). However, MBE suggests that iCOR-derived  $R_{rs}$  is biased high across the spectrum (ESM Fig. S2, MBE). Like the MBE results, overestimation of iCOR-derived  $R_{rs}$  was generally observed across the visible spectrum for the ESA Sentinel-2 Multi Spectral Imager (MSI) data in the Baltic Sea and a number of European inland waters (Warren et al., 2019). Warren et al. (2019) suggested that this under-correction of atmospheric effects in iCOR is due to the methodology of the algorithm to estimate the aerosol model. This methodology relies on the presence of land pixels in the scene. A summary of statistical indicators

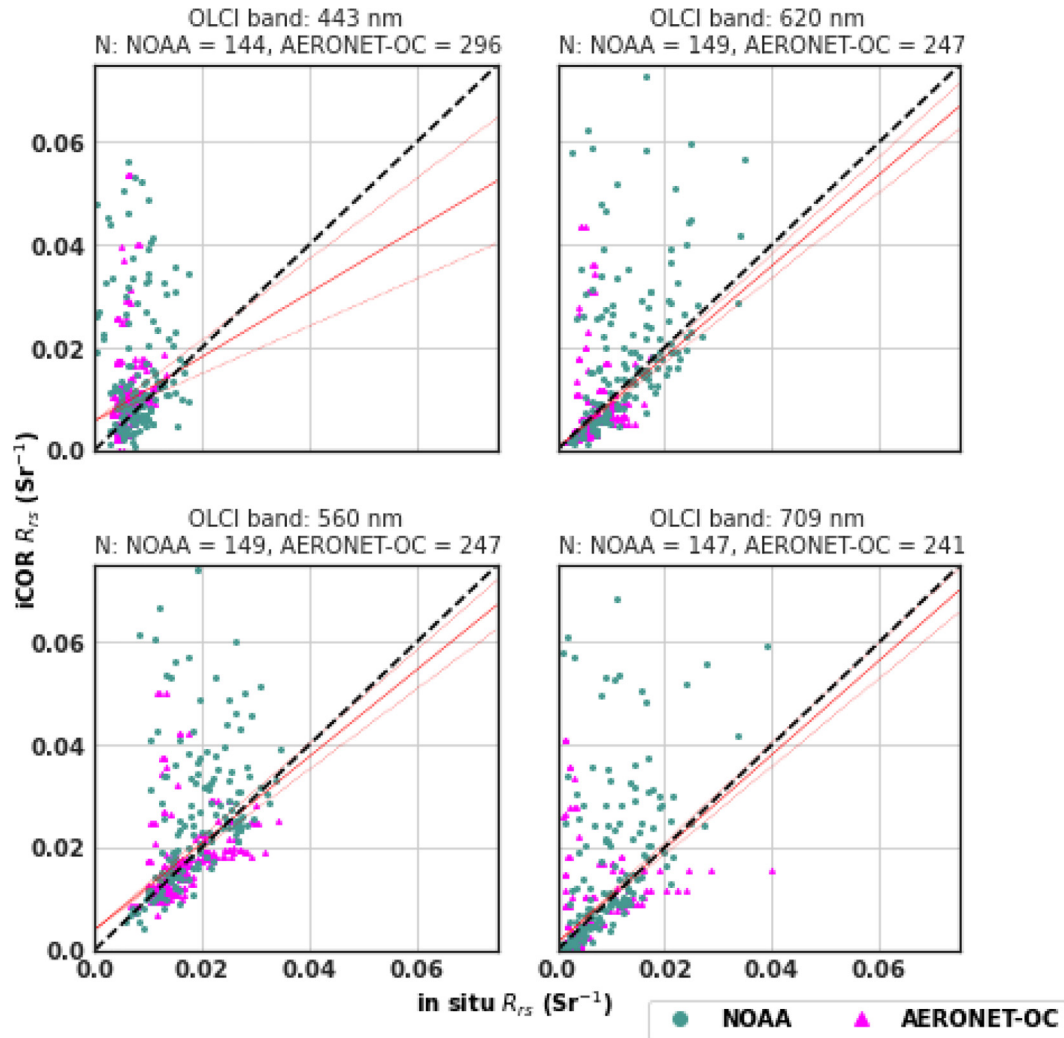


**Fig. 5.** Scatterplots of *iCOR*-derived  $R_{rs}$  versus *in situ*  $R_{rs}$  for selected OLCI bands. The dashed line is the 1:1 relation line. Red line is the Theil-Sen estimator slope with 90% confidence shown in the dashed red lines. Matchup data from AERONET-OC sites and NOAA-GLERL monitoring stations are plotted in pink and teal, respectively. (For interpretation of the references to color in this figure legend, the reader is referred to the web version of this article.)

estimated for each OLCI band to evaluate the performance of *iCOR* in retrieving  $R_{rs}$  values is presented in ESM Fig. S2. Results show that *iCOR* produced the lowest SSPB (-1.25 %), MdSA (16.91 %), MSA (31.14 %), RMSLE (0.18), and MAPE (38.03 %) values for the 560 nm band. The highest estimates for SSPB, MdSA, MSA, MBE,

and MAPE were estimated for the OLCI band at 412 nm with values of 83.26 %, 96.63 %, and 124.32 %,  $0.007 \text{ sr}^{-1}$  and 254 %, respectively.

*MDN-retrieved products.* MDN was applied to *iCOR*-corrected  $R_{rs}$  to estimate Chla and PC. The retrievals against the field-measured

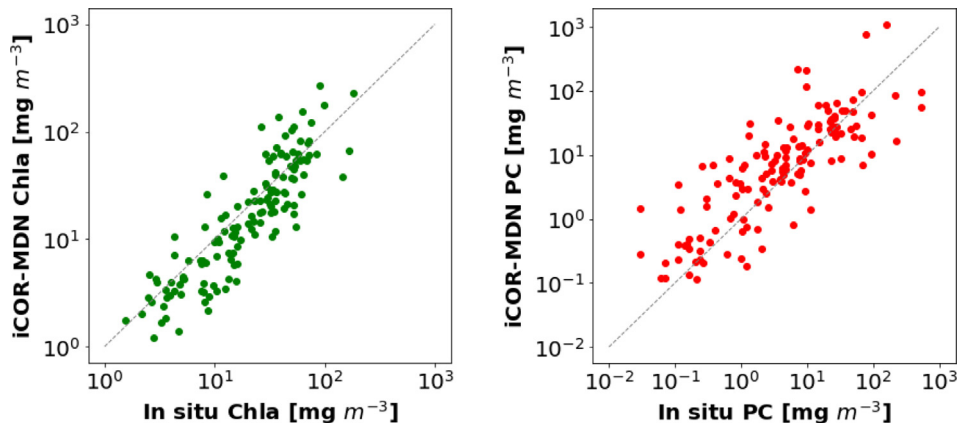


**Fig. 6.** Evaluation of MDN-derived Chla (left) and PC (right) applied to *iCOR*-corrected OLCI bands. The Theil-Sen estimator slope with 90% confidence is reported for each plot. The dashed line is the 1:1 relation line.

**Table 3**  
Performance of MDN in estimating Chla and PC from iCOR-corrected OLCI data.

	N	SSPB (%)	MdSA (%)	MSA (%)	RMSLE	MBE [ $\text{mg m}^{-3}$ ]	RMSE [ $\text{mg m}^{-3}$ ]	MAPE (%)	Slope
<b>Chla</b>	137	-22.71	45.53	63.66	0.27	1.33	29.33	47.08	0.86
<b>PC</b>	137	49.53	114.45	176.57	0.58	8.07	119.61	300.31	0.98

values are plotted in Fig. 6. The final iCOR matchup dataset had an average *in situ* Chla and PC of  $28.65 \pm 28.70 \text{ mg m}^{-3}$  and  $21.98 \pm 68.08 \text{ mg m}^{-3}$ , respectively. MDN estimated Chla and PC with RMSLE values of 0.27 and 0.58 from iCOR-corrected OLCI bands, respectively. Despite the large uncertainties in PC retrievals, the predictions exhibit a linear correspondence with *in situ* PC across three orders of magnitude of concentrations, i.e., 0.1 – 100  $\text{mg m}^{-3}$ . The performance indicators are summarized in Table 3.

#### ACOLITE

**Atmospheric correction.** A batch of 97 OLCI images processed with ACOLITE had concurrent *in situ* measurements. The number of concurrent *in situ* measurements of radiometric data, Chla, and PC with ACOLITE-corrected OLCI overpasses between 2016 and 2019 in WLE was 214. All ACOLITE-produced flags were used to exclude invalid pixels. 152 matchups were collected from the AERONET station with no field measurements of Chla, PC, and OLCI bands at 674, 754, and 779 nm. In the ACOLITE matchup dataset, there

were 40 samples with no measurements of OLCI bands at 510, 560, 620, 682, or 709 nm, collected from the AERONET station.

Fig. 7 shows ACOLITE- $R_{rs}$  values plotted against the *in situ* measurements for selected OLCI bands. ACOLITE produced  $R_{rs}$  for all OLCI bands shorter than 780 nm except 761, and 764. ESM Fig. S4 summarizes the performance assessment of ACOLITE in estimating  $R_{rs}$  for different OLCI bands. ACOLITE produced the lowest SSPB, MdSA, MSA, RMSLE, MBE, RMSE, and MAPE for bands centered at 665, 674 and 682 nm with values of 21–47 %, 21–47 %, 32–49.5 %, 0.16–0.20, 0.0029–0.0044  $\text{sr}^{-1}$ , 0.0036–0.0055  $\text{sr}^{-1}$ , and 37–54 %, respectively. This is expected as DSF approximates aerosol contributions by optimizing retrievals at a selected red band. ACOLITE performed poorly in estimating  $R_{rs}$  for OLCI band at 412 nm with SSPB, MdSA, MSA, RMSLE, and MAPE values of 81 %, 81 %, 90 %, 0.32, and 105 %, respectively. The high bias across all bands, as seen in the matchups (SSPB, Fig. S4), may be partially explained by the double correction for gas transmittance and also lack of EUMETSAT SVC gains being applied to the OLCI imagery by

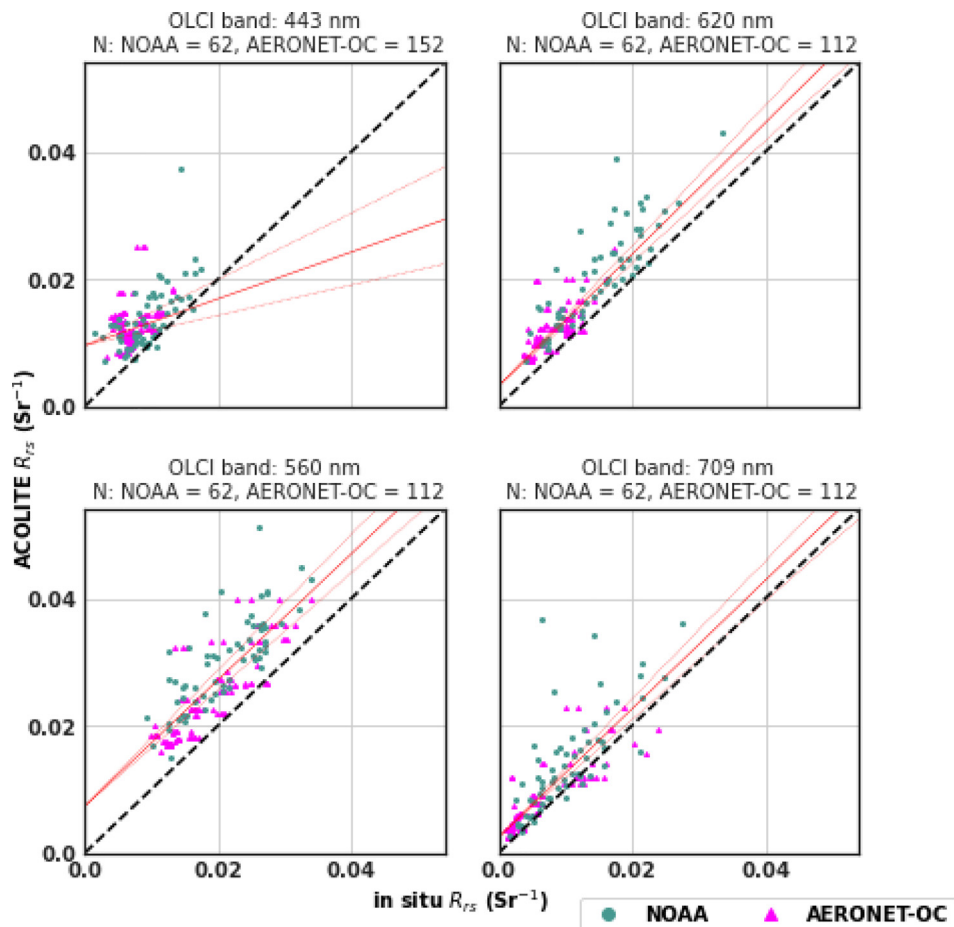


**Fig. 7.** Scatterplots of ACOLITE-derived  $R_{rs}$  versus *in situ*  $R_{rs}$  for selected OLCI bands. The dashed line is the 1:1 relation line. Red line is the Theil-Sen estimator slope with 90% confidence shown in the dashed red lines. Matchup data from AERONET-OC sites and NOAA-GLERL monitoring stations are plotted in pink and teal respectively. (For interpretation of the references to color in this figure legend, the reader is referred to the web version of this article.)

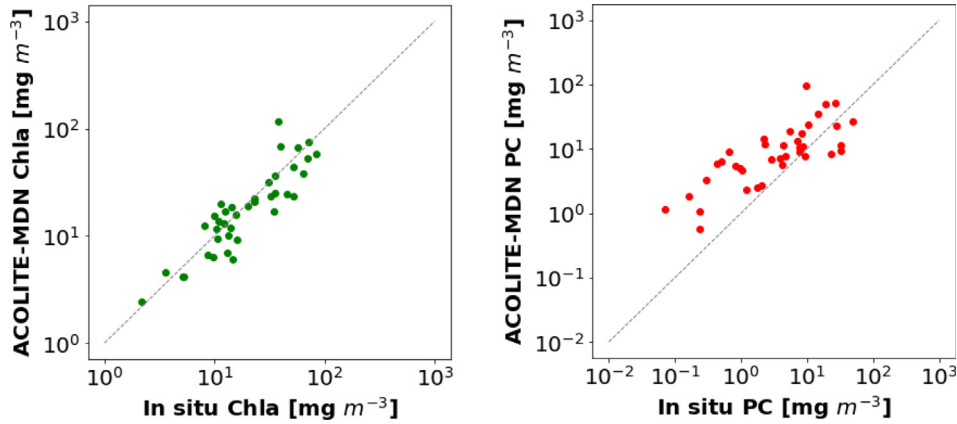


**Fig. 8.** Evaluation of MDN-derived Chla (left) and PC (right) applied to ACOLITE-corrected OLCI bands. The Theil-Sen estimator slope with 90% confidence is reported for each plot. The dashed line is the 1:1 relation line.

**Table 4**

Performance of MDN in estimating Chla and PC from ACOLITE-corrected OLCI data.

	N	SSPB (%)	MdSA (%)	MSA (%)	RMSLE	MBE [ $\text{mg m}^{-3}$ ]	RMSE [ $\text{mg m}^{-3}$ ]	MAPE (%)	Slope
<b>Chla</b>	39	-12.15	29.62	38.92	0.18	-1.21	16.57	32.66	0.74
<b>PC</b>	39	132.8	141.99	211.29	0.6	5.27	17.57	331.51	0.95

the version of ACOLITE used to process these matchups (see ACOLITE in Methods and datasets section).

**MDN-retrieved products.** In the matchup dataset finalized for the ACOLITE processing, Chla and PC have average values of  $27.82 \pm 2.083 \text{ mg m}^{-3}$  and  $12.85 \pm 24.58 \text{ mg m}^{-3}$ , respectively. MDN-retrieved Chla and PC products from ACOLITE-corrected OLCI bands are plotted in Fig. 8. Results show that Chla and PC are estimated with RMSLE values of 0.18 and 0.6, respectively. Table 4 summarizes the statistical indicators for MDN performance in retrieving Chla and PC from ACOLITE data.

#### POLYMER

**Atmospheric correction.** A batch of 98 OLCI scenes acquired over WLE had concurrent *in situ* measurements and was processed with the POLYMER. The number of concurrent *in situ* measurements of Chla, PC, and radiometric data with POLYMER-corrected OLCI overpasses between 2016 and 2019 in WLE was 260. The pixels with the POLYMER “out\_of\_bounds” flags were excluded from further analysis. 175 matchups were collected from the AERONET station with no field measurements of Chla, PC and OLCI bands at 674, 754, and 779 nm. There were no measurements of OLCI bands at 510, 560, 620, 682, 709 nm for the 49 matchups collected from the AERONET station.

POLYMER- $R_{rs}$  values are plotted against the *in situ* measurements in Fig. 9 for selected OLCI bands. POLYMER produced the  $R_{rs}$  values for all OLCI bands shorter than 780 nm except 761 nm. POLYMER underestimates  $R_{rs}$  in all bands. Values at OLCI bands 761 and 764 were all negative. A summary of POLYMER performance in retrieving  $R_{rs}$  values in different OLCI bands is provided in ESM Fig. S6. Errors for the longer OLCI bands are larger than the ones for shorter bands. The smallest MdSA, MSA, RMSLE, and MAPE are for  $R_{rs}(560 \text{ nm})$ , with values of 27 %, 27 %, 0.13, and 21 %, respectively. SSPB and MBE are the lowest for the blue band at 412 nm with values of -10 %,  $-0.0002 \text{ sr}^{-1}$ , respectively.

**MDN-retrieved products.** In the POLYMER matchup dataset, Chla and PC have average values of  $23.37 \pm 20.76 \text{ mg m}^{-3}$  and  $9.70 \pm 2.173 \text{ mg m}^{-3}$ , respectively. MDN was applied to POLYMER-derived  $R_{rs}$  from OLCI imagery to estimate Chla and PC. The satellite-derived estimates are plotted against the field-measured Chla and PC in Fig. 10. Results demonstrate that MDN can estimate Chla and PC with RMSLE values of 0.43 and 0.57, respectively. PC estimates below  $10^{-1}$  (or above  $10^3$ ) are outside the range of the training dataset, and are therefore extrapolated by the MDN, but are included here for completeness. The performance indicators are summarized in Table 5.

#### Performance comparison

Common matchups between the three AC algorithms, that have *in situ* measurements of  $R_{rs}$ , Chla and PC and valid atmospherically-corrected  $R_{rs}$  and MDN estimation were extracted to produce the plots in Fig. 11, Fig. 12, and Fig. 14.

#### Atmospheric correction algorithms

The common *in situ* datasets were used to compare the performance of the AC algorithms. The number of matchups in each band is different. Fig. 11 shows a comparison between the median  $R_{rs}$  values in each band derived from *in situ* data and AC algorithms. The spectral shape of all three atmospherically corrected data is similar to the *in situ* data; however, iCOR (SAM =  $0.093\pi$ ) and ACOLITE (SAM =  $0.065\pi$ ) tend to agree more with the *in situ*  $R_{rs}$  data (Fig. 11; SAM for POLYMER is  $0.132\pi$ ). The scatterplots of  $R_{rs}$  data derived from each AC algorithm is plotted against the field-measured data in ESM Fig. S7 for all OLCI bands.

Fig. 12 compares the performance of different algorithms using the estimated statistical indicators. POLYMER underestimated all OLCI bands with negative SSPB and MBE values. iCOR underestimated  $R_{rs}$  for bands longer than 443 nm with negative SSPB values. ACOLITE had positive SSPB and MBE values in all OLCI bands. iCOR had the lowest MdSA values for bands between 443 and 620 nm (and the lowest MSA and RMSLE values for bands between 490

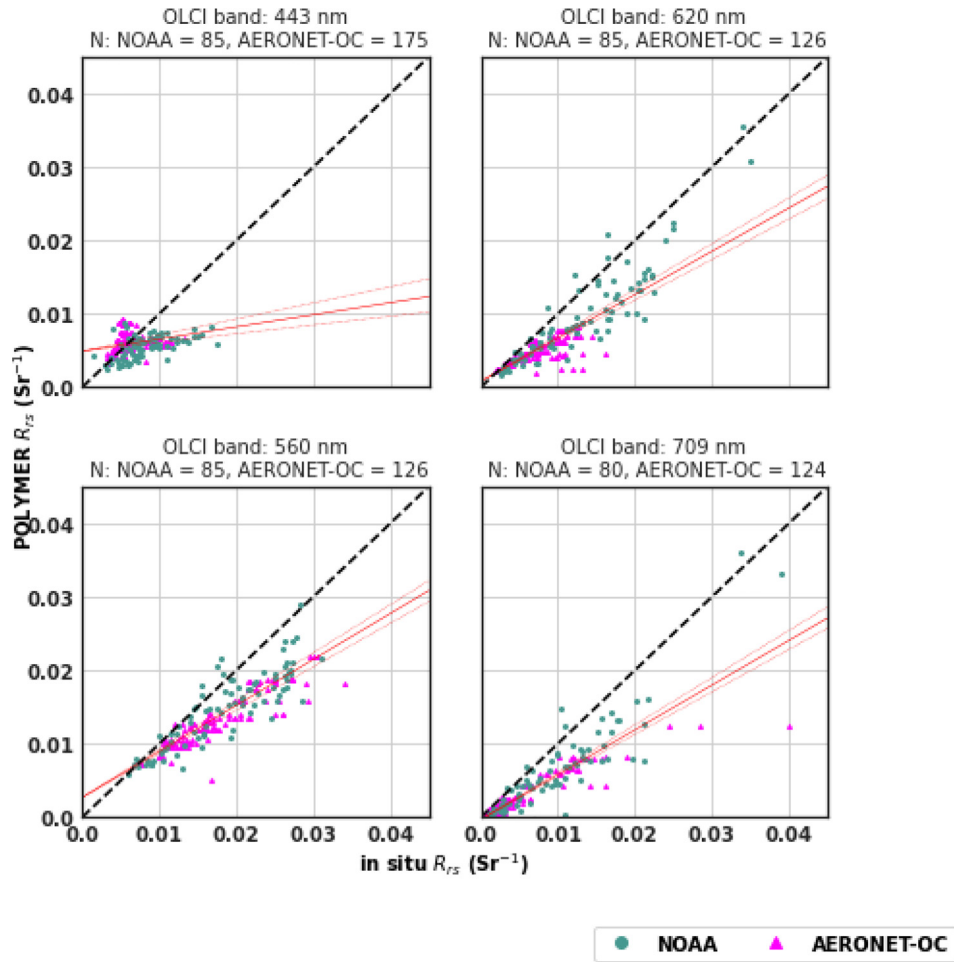


**Fig. 9.** Scatterplots of POLYMER-derived  $R_{rs}$  versus *in situ*  $R_{rs}$  for selected OLCI bands. The dashed line is the 1:1 relation line. Red line is the Theil-Sen estimator slope with 90% confidence shown in the dashed red lines. Matchup data from AERONET-OC sites and NOAA-GLERL monitoring stations are plotted in pink and teal, respectively. (For interpretation of the references to color in this figure legend, the reader is referred to the web version of this article.)

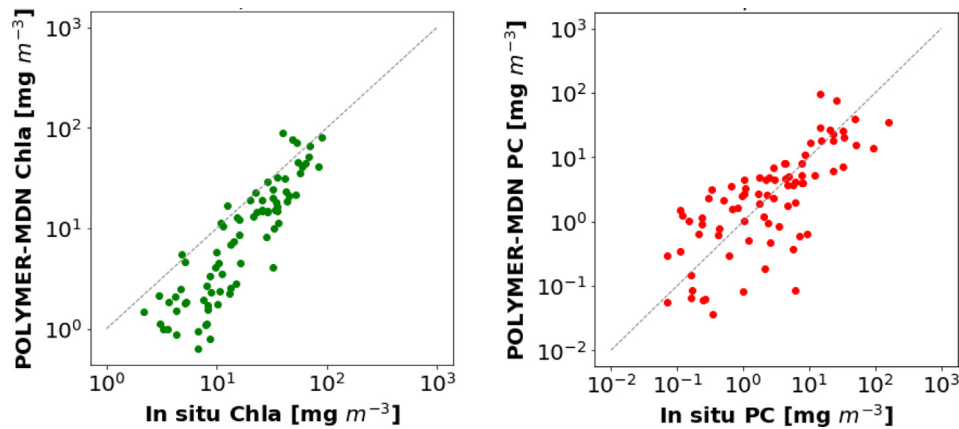


**Fig. 10.** Evaluation of MDN-derived Chla (left) and PC (right) applied to POLYMER-corrected OLCI bands. The Theil-Sen estimator slope with 90% confidence is reported for each plot. The dashed line is the 1:1 relation line.

**Table 5**  
Performance of MDN in estimating Chla and PC from POLYMER-corrected OLCI data.

	N	SSPB (%)	MdSA (%)	MSA (%)	RMSLE	MBE [ $\text{mg m}^{-3}$ ]	RMSE [ $\text{mg m}^{-3}$ ]	MAPE (%)	Slope
<b>Chla</b>	80	-99.37	102.51	129.92	0.44	-7.83	14.1	50.69	0.64
<b>PC</b>	80	2.21	137.45	183.11	0.58	-2.18	20.82	146.43	0.63

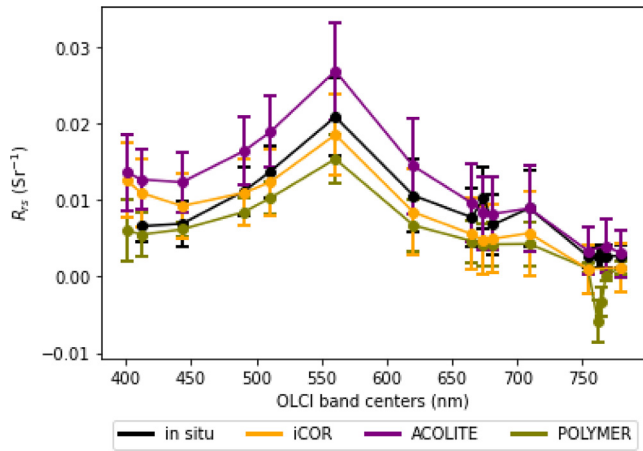


**Fig. 11.** Median of hyperspectral (NOAA-GLERL) *in situ*  $R_{rs}$  and the ones processed with different AC algorithms at each OLCI band. Error bars represent the standard deviation at each OLCI band.

and 620 nm) compared to ACOLITE and POLYMER. ACOLITE and iCOR perform closely at 620 and 665 nm in terms of MdSA and RMSLE values, while outperforming POLYMER MdSA and RMSLE results at these two bands (Table 6 and Table 7). For bands

between 674 and 709 nm ACOLITE performs best compared to iCOR and POLYMER with the lowest MdSA, MSA, and RMSLE values. For the shortest (412 and 443 nm) and the longest bands (754 and 779 nm), POLYMER performed best in terms of all statistical indicators (except SSPB for longer ones).

*Pigment retrievals*

MDN was applied to iCOR-, ACOLITE-, and POLYMER-corrected OLCI image acquired on 29 Aug 2016 to produce Chla (upper plots) and PC (lower plots) maps (Fig. 13). The spatial pattern of each product is the same between the three AC algorithms, showing high values of Chla and PC in Sandusky Bay and at the mouth of the Maumee River, which is the main source of nutrient loading each year (Moore et al., 2019). This pattern agrees well with previous studies (Binding et al., 2019; O’Shea et al., 2021). MDN applied to ACOLITE did not return any values close to the shoreline. MDN applied to POLYMER and iCOR returned a fewer number of PC retrievals in relatively clear waters. This is likely because PC estimates  $< 10^{-1}$  (or above  $10^3$ ) are outside the range of the MDN’s training dataset (O’Shea et al., 2021).

A comparison between statistical indicators estimated from the application of MDN to different AC algorithms is shown in Fig. 14. With the limited size matchup dataset derived in this study, ACOLITE outperformed other algorithms in terms of indicators in the

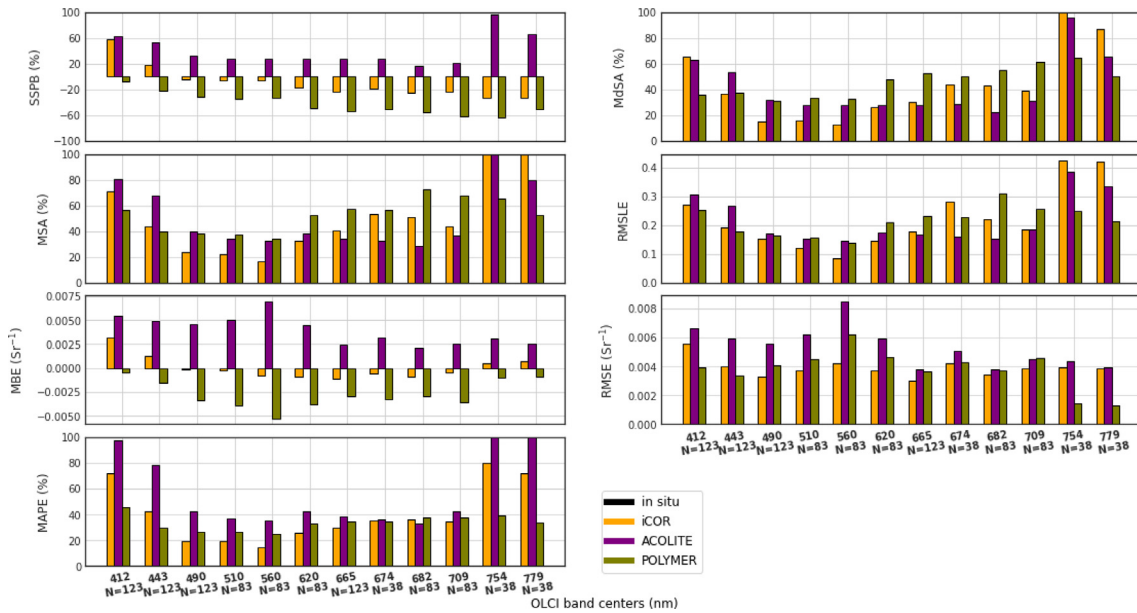


**Fig. 12.** Comparison of iCOR, ACOLITE, and POLYMER performances in estimating  $R_{rs}$  values, using NOAA-GLERL and AERONET-OC *in situ* data, in different OLCI bands. The number of matchups for each band is shown in the second line of y-axis labels.

**Table 6**  
MdSA (%) values for each AC model in retrieving  $R_{rs}$  values at 620 and 665 nm bands.

OLCI band centers (nm)	iCOR	ACOLITE	POLYMER	N
620	26.34	27.62	48.15	83
665	30.43	27.82	52.97	123

**Table 7**  
RMSLE values for each AC model in retrieving  $R_{rs}$  values at 620 and 665 nm bands.

OLCI band centers (nm)	iCOR	ACOLITE	POLYMER	N
620	0.15	0.17	0.21	83
665	0.18	0.17	0.23	123

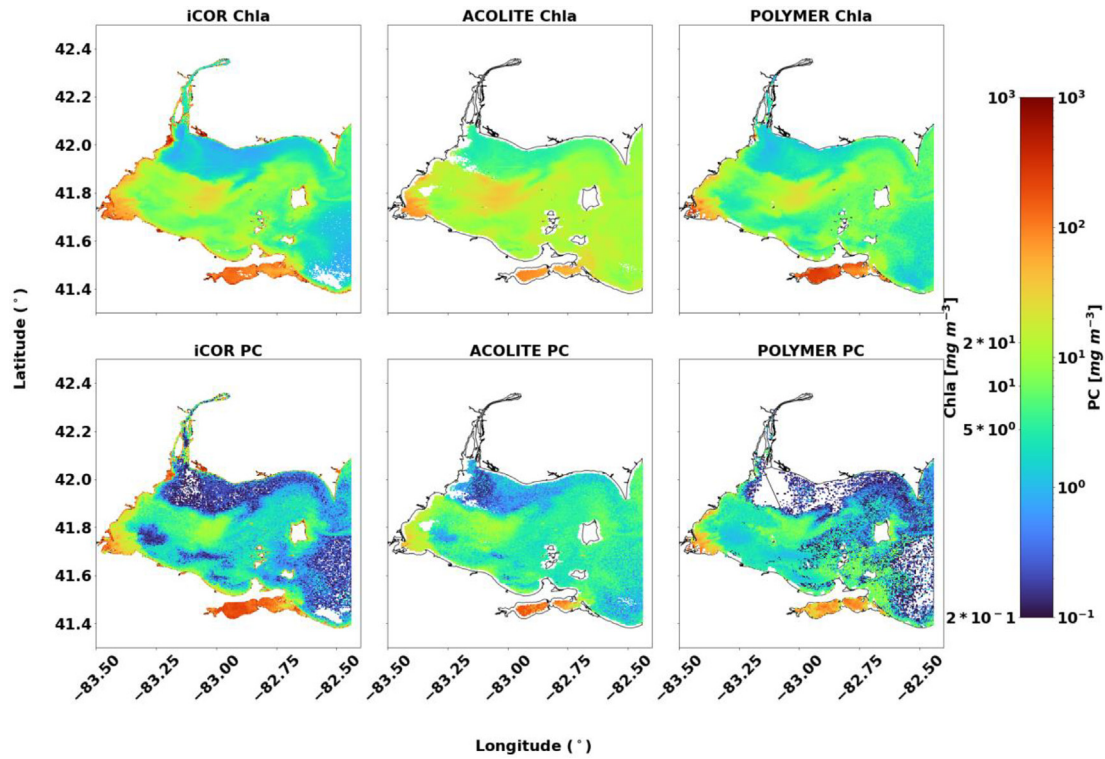


**Fig. 13.** Chla (upper) and PC (lower) maps (in logarithmic scale) on 29 August 2016, derived from the application of MDN to iCOR, ACOLITE, and POLYMER, respectively, from left to right. Chla and PC values larger than  $1000 \text{ mg m}^{-3}$  are masked out in the maps.

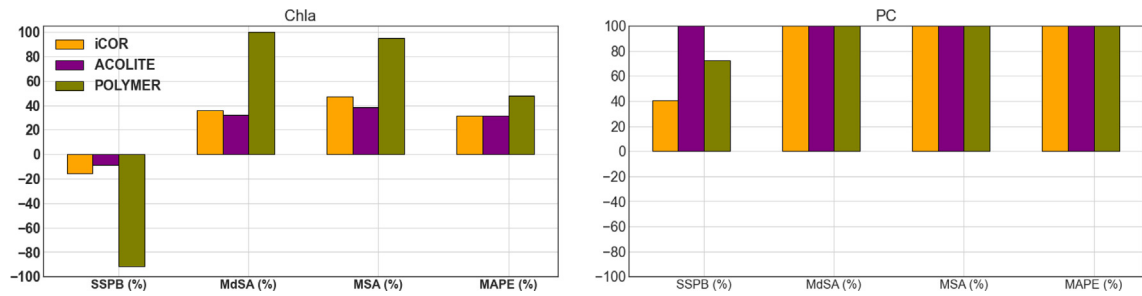


**Fig. 14.** Comparison of MDN-derived Chla and PC from iCOR-, ACOLITE-, and POLYMER-corrected Rrs values. The matchup size for all three AC algorithms is 26. Values larger than 100% are not shown in PC plot.

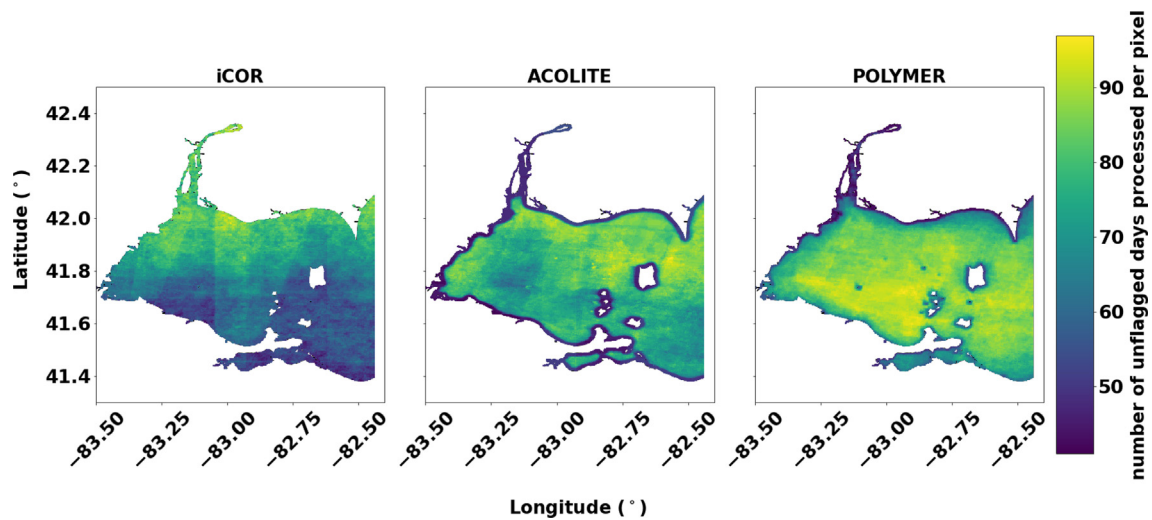


**Fig. 15.** The total number of processed days per pixel, summed for 2016–2019 OLCI images common between the three AC algorithms.

estimation of Chla with a marginal improvement compared to iCOR. However, MDN performed poorly in retrieving PC from OLCI bands, regardless of the AC algorithm applied.

## Discussion

The Evaluation Section presented the performance of each AC algorithm (iCOR, ACOLITE, and POLYMER) separately, using the matchup data processed by assessing valid (unflagged) pixels in each algorithm. However, the flags in each AC algorithm are different, leading to varying matchup datasets. Therefore, in the Performance comparison section above, a common matchup dataset was assembled to enable the comparison between algorithms. Particularly, the overall performance of iCOR improved when statistical

indicators were computed from the matchups common to ACOLITE and POLYMER. This corroborates inadequacy of iCOR's cloud-masking approach. To compare the derived flags in the three different AC processors, the spatial variability of valid pixels in each algorithm is mapped in Fig. 15 (before producing the common matchup). The maps reveal that both iCOR and ACOLITE have fewer valid products compared to POLYMER. iCOR has the least valid pixels for the western and southern part of WLE, which is usually characterized by higher concentrations of algal blooms. ACOLITE contains the least number of valid pixels close to the lake shoreline. Therefore, it is expected that the impact of radiance originating from adjacent land (adjacency effect) is less severe in the remaining pixels, as the pixels with the most severe adjacency effects were removed. Removal of pixels that contain severe adja-

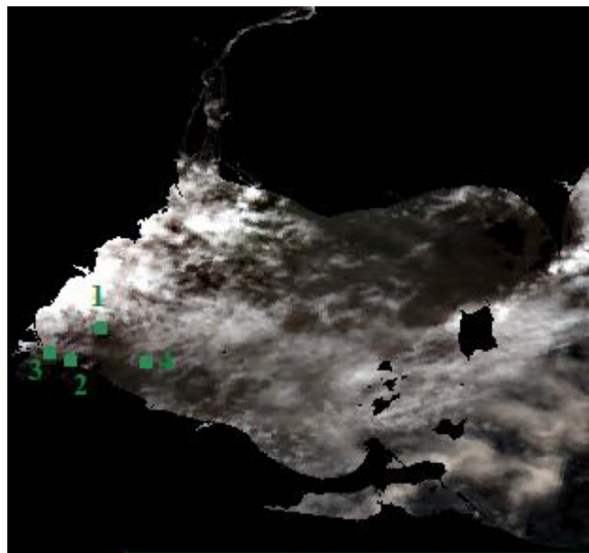
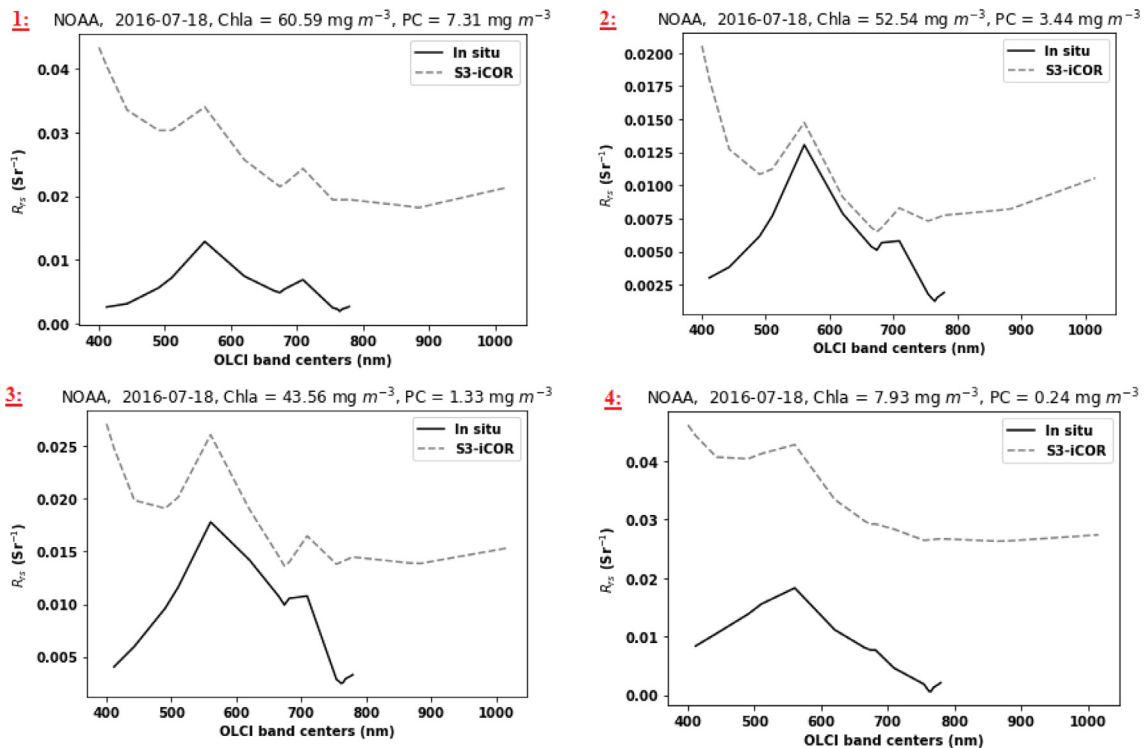


**Fig. 16.** An example of a day (18 July 2016) when the locations of NOAA-GLERL stations were covered by cloud (or cloud shadows); however, the iCOR processor was not able to flag them. The locations of NOAA-GLERL stations are shown in green (bottom). The  $R_{rs}$  spectra in each station measured by NOAA-GLERL and estimated by iCOR processor are also plotted (top). (For interpretation of the references to color in this figure legend, the reader is referred to the web version of this article.)

gency effects is especially essential for small lakes with complex geometries (Pan et al., 2022).

The cloud mask in the iCOR processor does not reliably identify clouds or cloud shadows. For instance, the OLCI image acquired on 18 July 2016 is cloudy. ACOLITE and Idepix in POLYMER processor have masked out pixels located around NOAA-GLERL monitoring stations and AERONET-OC sites due to clouds or cloud shadows. Therefore, no matchups have been produced on this date for these two AC algorithms. However, iCOR matchup has picked up those pixels, as it is plotted in Fig. 16.

Once a common matchup dataset is used among the three processors, Fig. 11 demonstrates that the median iCOR-derived  $R_{rs}$  follow the shape of the median *in situ* spectra in the green – NIR range more closely than the other two processors. Pahlevan et al. (2021) also suggested iCOR as one of the top performers in turbid/eutrophic waters.

Large inaccuracies in PC retrievals exist regardless of the selected AC processor. These inaccuracies are due to a combination of multiple factors, including uncertainties in training data (i.e., both *in situ* PC and  $R_{rs}$ ) (O'Shea et al., 2021), inaccuracies in satellite-derived  $R_{rs}$ , lack of the PC fluorescence feature (a band centered at 650 nm; Zolfaghari et al., 2021) in OLCI and, in general, subtle relevant spectral features with respect to those of Chla, which is the primary mediator of the shape of the spectrum. Through modeling efforts, Moses et al. (2012) demonstrated that the uncertainties in  $R_{rs}$ , resulting from sensor instrument noise, can propagate to errors as high as 80 % in the retrieved constituents' concentration (e.g., Chla) from Hyperspectral Imager for the Coastal Ocean (HICO) satellite sensor in optically complex waters. The uncertainties in  $R_{rs}$  can also result from the AC approaches (Ibrahim et al., 2018). Pahlevan et al. (2021) showed that for multispectral sensors, the combination of uncertainties from instrument noise and AC could result in 25–70 % errors in the estimated products. Similarly, investigating the impact of uncertainties in *in situ*  $R_{rs}$  measurements on the PC retrievals from satellite-derived  $R_{rs}$  is essential (O'Shea et al., 2021). Other phytoplankton pigments can also influence the accuracy of PC estimation. Simis et al. (2007) discussed the impact of pigments (e.g., Chlb, Chlc, and pheophytin) on PC retrievals, especially at low concentrations, using a band-ratio algorithm applied to MERIS (Simis et al., 2005). Therefore, the existing literature suggests that the retrieval accuracy of PC from multispectral satellites can depend on multiple factors, including the PC range of values and concentrations of other phytoplankton pigments whose signals either overlap with PC or are not well captured with current multispectral sensors (Zolfaghari et al., 2021). Despite the aforementioned uncertainties, PC predictions from iCOR-derived  $R_{rs}$  are found to exhibit a linear correspondence with *in situ* PC across the 0.1 – 100 mg m<sup>-3</sup> range in this study. On the other hand, Chla predictions from MDNs applied to iCOR-derived  $R_{rs}$  appear to contain acceptable uncertainties (<50 %), suggesting that this processing scheme could prove viable for highly eutrophic aquatic ecosystems.

## Conclusion

The evaluation of iCOR, ACOLITE, and POLYMER AC algorithms has been performed for OLCI satellite data acquired over eutrophic waters of the western Lake Erie in 2016–2019. Field measurements of radiometric data collected concurrently with satellite images were used to assess the quality of iCOR-, ACOLITE-, and POLYMER-retrieved  $R_{rs}$  products. The atmospherically corrected OLCI images were then used as input into MDN to estimate Chla and PC. Employing a common matchup dataset showed that MDN applied to iCOR and ACOLITE performs better in retrieving

Chla, compared to POLYMER, with MDN applied to ACOLITE providing marginal improvements compared to MDN applied to iCOR. Large uncertainties (MdSA > 100 %) were observed in PC retrieval from MDN application to the three selected AC processors, underscoring the higher sensitivity of MDNs to the fidelity of input  $R_{rs}$  spectra. The performance of each algorithm in estimating  $R_{rs}$  is dependent on the wavelength. For OLCI bands between 490 and 709 nm, iCOR and ACOLITE outperform POLYMER, while POLYMER performs best for bands shorter than 490 nm and longer than 709 nm. The standalone evaluation of MDN applied to each AC processor shows that MDN, in combination with the application of iCOR, can produce a larger number of valid estimates for Chla with a MdSA value of 45.53 %. Therefore, iCOR being a fully self-contained method which is suitable for operational monitoring programs, this study suggests that MDN in combination with iCOR provides a practical workflow for estimating Chla from OLCI data. The iCOR's handling of cloud (and cloud shadow) detection needs further analysis and improvements.

The MDN code for OLCI can be accessed via <https://github.com/STREAM-RS>.

## Declaration of Competing Interest

The authors declare that they have no known competing financial interests or personal relationships that could have appeared to influence the work reported in this paper.

## Acknowledgments

This research was undertaken thanks in part to funding from the Canada First Research Excellence Fund through the Transformative Sensor Technologies and Smart Watershed project within the Global Water Futures program. Funding supports through the NASA grant #80NSSC20M0235, PACE Science and Applications Team, and the USGS Landsat Science Team Award #140G0118C0011 are also acknowledged. POLYMER-corrected data were generated at PML (Plymouth Marine Laboratory) by Nick Selmes, for the Copernicus Land Monitoring Service (CLMS). ACOLITE products were processed by Arun Saranathan with SSAIL. Sentinel-3 OLCI data were also processed by EarthConsole® service ([www.earthconsole.eu](http://www.earthconsole.eu)) with iCOR4S3 atmospheric correction. The project was supported by ESA Network of Resources (NoR) Initiative. We acknowledge NASA's AERONET team for maintaining the network. Our greatest appreciation is extended to the AERONET-OC Principal Investigators (Timothy Moore, Menghua Wang, Steve Ruberg) and their corresponding funding agencies. The authors are also thankful to Steve Ruberg for providing the NOAA-GLERL field data of WLE.

## Appendix A. Supplementary data

Supplementary data to this article can be found online at <https://doi.org/10.1016/j.jglr.2022.12.010>.

## References

- Bailey, S.W., Werdell, P.J., 2006. A multi-sensor approach for the on-orbit validation of ocean color satellite data products. *Remote Sens. Environ.* 102, 12–23. <https://doi.org/10.1016/j.rse.2006.01.015>.
- Baker, D.B., Confesor, R., Ewing, D.E., Johnson, L.T., Kramer, J.W., Merryfield, B.J., 2014. Phosphorus loading to Lake Erie from the Maumee, Sandusky and Cuyahoga rivers: the importance of bioavailability. *J. Great Lakes Res.* 40, 502–517. <https://doi.org/10.1016/j.jglr.2014.05.001>.
- Binding, C.E., Jerome, J.H., Bukata, R.P., Booty, W.G., 2010. Suspended particulate matter in Lake Erie derived from MODIS aquatic colour imagery. *Int. J. Remote Sens.* 31, 5239–5255. <https://doi.org/10.1080/01431160903302973>.

- Binding, C.E., Greenberg, T.A., Bukata, R.P., 2012. An analysis of MODIS-derived algal and mineral turbidity in Lake Erie. *J. Great Lakes Res.* 38, 107–116. <https://doi.org/10.1016/j.jglr.2011.12.003>.
- Binding, C.E., Zastepa, A., Zeng, C., 2019. The impact of phytoplankton community composition on optical properties and satellite observations of the 2017 western Lake Erie algal bloom. *J. Great Lakes Res.* 45, 573–586. <https://doi.org/10.1016/j.jglr.2018.11.015>.
- Binding, C.E., Pizzolato, L., Zeng, C., 2021. EOLakeWatch: delivering a comprehensive suite of remote sensing algal bloom indices for enhanced monitoring of Canadian eutrophic lakes. *Ecol. Ind.* 121. <https://doi.org/10.1016/j.ecolind.2020.106999> 106999.
- Bishop, C.M., 1994. Mixture Density Networks. NCRG/94/004. Aston University Birmingham. [https://doi.org/10.1007/978-3-322-81570-5\\_8](https://doi.org/10.1007/978-3-322-81570-5_8).
- de Keukelaere, L., Sterckx, S., Adriaensen, S., Bhatia, N., Monbaliu, J., Toorman, E., Cattrijse, A., Lebreton, C., der Zande, D., van Knaeps, E., 2020. Coastal turbidity derived from PROBA-V global vegetation satellite. *Remote Sensing* 2020, Vol. 12, Page 463 12, 463. <https://doi.org/10.3390/RS12030463>.
- de Keukelaere, L., Sterckx, S., Adriaensen, S., Knaeps, E., Reusen, I., Giardino, C., Bresciani, M., Hunter, P., Neil, C., van der Zande, D., Vaiciute, D., 2018. Atmospheric correction of Landsat-8/OLI and Sentinel-2/MSI data using iCOR algorithm: validation for coastal and inland waters. *Eur J Remote Sens* 51, 525–542. <https://doi.org/10.1080/22797254.2018.1457937>.
- Doerffer, R., Schiller, H., 2007. The MERIS case 2 water algorithm. *Int. J. Remote Sens.* 28, 517–535. <https://doi.org/10.1080/01431160600821127>.
- Fay, L.A., Herdendorf, C.E., 1984. Environmental sensitivity index (ESI) maps for the Lake Erie system / prepared by Laura A. Fay and Charles E. Herdendorf.
- Giannini, F., Hunt, B.P.V., Jacoby, D., Costa, M., 2021. Performance of OLCI Sentinel-3A satellite in the Northeast Pacific coastal waters. *Remote Sens. Environ.* 256. <https://doi.org/10.1016/j.rse.2021.112317> 112317.
- Gower, J., King, S., Borstad, G., Brown, L., 2008. The importance of a band at 709 nm for interpreting water-leaving spectral radiance. *Can. J. Remote. Sens.* 34, 287–295. <https://doi.org/10.5589/m08-022>.
- Ibrahim, A., Franz, B., Ahmad, Z., Healy, R., Knobelspiesse, K., Gao, B.C., Proctor, C., Zhai, P.W., 2018. Atmospheric correction for hyperspectral ocean color retrieval with application to the Hyperspectral Imager for the Coastal Ocean (HICO). *Remote Sens. Environ.* 204, 60–75. <https://doi.org/10.1016/j.rse.2017.10.041>.
- Ilori, C.O., Knudby, A., 2020. An approach to minimize atmospheric correction error and improve physics-based satellite-derived bathymetry in a coastal environment. *Remote Sensing* 2020, Vol. 12, Page 2752 12, 2752. <https://doi.org/10.3390/RS12172752>.
- Kotchenova, S.V., Vermote, E.F., Levy, R., Lyapustin, A., 2008. Radiative transfer codes for atmospheric correction and aerosol retrieval: intercomparison study. *Applied Optics*, Vol. 47, Issue 13, pp. 2215–2226 47, 2215–2226. <https://doi.org/10.1364/AO.47.002215>.
- Kravitz, J., Matthews, M., Bernard, S., Griffith, D., 2020. Application of Sentinel 3 OLCI for chl-a retrieval over small inland water targets: Successes and challenges. *Remote Sens. Environ.* 237. <https://doi.org/10.1016/j.rse.2019.111562> 111562.
- Liu, X., Steele, C., Simis, S., Warren, M.A., Tyler, A., Spyarakos, E., Selmes, N., Hunter, P., 2021. Retrieval of Chlorophyll-a concentration and associated product uncertainty in optically diverse lakes and reservoirs. *Remote Sens. Environ.* 267. <https://doi.org/10.1016/j.rse.2021.112710> 112710.
- Maciel, F.P., Pedocchi, F., 2022. Evaluation of ACOLITE atmospheric correction methods for Landsat-8 and Sentinel-2 in the Río de la Plata turbid coastal waters. *Int. J. Remote Sens.* 43, 215–240. <https://doi.org/10.1080/01431161.2021.2009149>.
- Mancino, G., Console, R., Greco, M., Iacovino, C., Trivigno, M.L., Falciano, A., 2022. Assessing vegetation decline due to pollution from solid waste management by a multitemporal remote sensing approach. *Remote Sensing* 2022, Vol. 14, Page 428 14, 428. <https://doi.org/10.3390/RS14020428>.
- Matthews, M.W., Bernard, S., Robertson, L., 2012. An algorithm for detecting trophic status (chlorophyll-a), cyanobacterial-dominance, surface scums and floating vegetation in inland and coastal waters. *Remote Sens. Environ.* 124, 637–652. <https://doi.org/10.1016/j.rse.2012.05.032>.
- Mobley, C.D., 1999. Estimation of the remote-sensing reflectance from above-surface measurements. *Appl. Opt.* 38, 7442. <https://doi.org/10.1364/ao.38.007442>.
- Mograne, M.A., Jamet, C., Loisel, H., Vantrepotte, V., Mériaux, X., Cauvin, A., 2019. Evaluation of five atmospheric correction algorithms over french optically-complex waters for the sentinel-3a ocli ocean color sensor. *Remote Sens. (Basel)* 11, 1–25. <https://doi.org/10.3390/RS11060668>.
- Moore, T.S., Feng, H., Ruberg, S.A., Beadle, K., Constant, S.A., Miller, R., Muzzi, R.W., Johengen, T.H., DiGiacomo, P.M., Lance, V.P., Holben, B.N., Wang, M., 2019. SeaPRISM observations in the western basin of Lake Erie in the summer of 2016. *J. Great Lakes Res.* 45, 547–555. <https://doi.org/10.1016/j.jglr.2018.10.008>.
- Morley, S.K., Brito, T., Welling, D.T., 2018. Measures of model performance based on the log accuracy ratio. *Space Weather* 16, 69–88. <https://doi.org/10.1002/2017SW001669>.
- Moses, W.J., Bowles, J.H., Lucke, R.L., Corson, M.R., 2012. Impact of signal-to-noise ratio in a hyperspectral sensor on the accuracy of biophysical parameter estimation in case II waters. *Opt. Express* 20, 4309. <https://doi.org/10.1364/oe.20.004309>.
- Müller, D., Krasemann, H., Brewin, R.J.W., Brockmann, C., Deschamps, P.Y., Doerffer, R., Fomferra, N., Franz, B.A., Grant, M.G., Groom, S.B., Mélin, F., Platt, T., Regner, P., Sathyendranath, S., Steinmetz, F., Swinton, J., 2015. The Ocean Colour Climate Change Initiative: II. Spatial and temporal homogeneity of satellite data retrieval due to systematic effects in atmospheric correction processors. *Remote Sens. Environ.* 162, 257–270. <https://doi.org/10.1016/j.rse.2015.01.033>.
- Neil, C., Spyarakos, E., Hunter, P.D., Tyler, A.N., 2019. A global approach for chlorophyll-a retrieval across optically complex inland waters based on optical water types. *Remote Sens. Environ.* 229, 159–178. <https://doi.org/10.1016/j.rse.2019.04.027>.
- O'Shea, R.E., Pahlevan, N., Smith, B., Bresciani, M., Egerton, T., Giardino, C., Li, L., Moore, T., Ruiz-Verdú, A., Ruberg, S., Simis, S.G.H., Stumpf, R., Vaičiūtė, D., 2021. Advancing cyanobacteria biomass estimation from hyperspectral observations: Demonstrations with HICO and PRISMA imagery. *Remote Sens. Environ.* 266. <https://doi.org/10.1016/j.rse.2021.112693> 112693.
- Pahlevan, N., Smith, B., Binding, C.E., Gurlin, D., Li, L., Bresciani, M., Giardino, C., 2020a. Hyperspectral retrievals of phytoplankton absorption and chlorophyll-a in inland and nearshore coastal waters. *Remote Sens. Environ.* 253. <https://doi.org/10.1016/j.rse.2020.112200> 112200.
- Pahlevan, N., Smith, B., Schalles, J., Binding, C., Cao, Z., Ma, R., Alikas, K., Kangro, K., Gurlin, D., Hà, N., Matsushita, B., Moses, W., Greb, S., Lehmann, M.K., Ondrusek, M., Oppelt, N., Stumpf, R., 2020b. Seamless retrievals of chlorophyll-a from Sentinel-2 (MSI) and Sentinel-3 (OLCI) in inland and coastal waters: A machine-learning approach. *Remote Sens. Environ.* 240. <https://doi.org/10.1016/j.rse.2019.111604> 111604.
- Pahlevan, N., Mangin, A., Balasubramanian, S., Smith, B., Alikas, K., Arai, K., Barbosa, C., Bélanger, S., Binding, C., Bresciani, M., Giardino, C., Gurlin, D., Fan, Y., Harmel, T., Hunter, P., Ishikawa, J., Kratzer, S., Lehmann, M.K., Ligi, M., Ma, R., Martin-Lauzer, F.R., Olmanson, L., Oppelt, N., Pan, Y., Peters, S., Reynaud, N., Sander de Carvalho, L.A., Simis, S., Spyarakos, E., Steinmetz, F., Stelzer, K., Sterckx, S., Tormos, T., Tyler, A., Vanhellefont, Q., Warren, M.A., 2021. ACIX-Aqua: A global assessment of atmospheric correction methods for Landsat-8 and Sentinel-2 over lakes, rivers, and coastal waters. *Remote Sens. Environ.* 258. <https://doi.org/10.1016/j.rse.2021.112366>.
- Pan, Y., Bélanger, S., Huot, Y., 2022. Evaluation of Atmospheric Correction Algorithms over Lakes for High-Resolution Multispectral Imagery: Implications of Adjacency Effect. *Remote Sensing* 2022, Vol. 14, Page 2979 14, 2979. <https://doi.org/10.3390/RS14132979>.
- Pereira-Sandoval, M., Ruescas, A., Urrego, P., Ruiz-Verdú, A., Delegido, J., Tenjo, C., Soria-Perpinya, X., Vicente, E., Soria, J., Moreno, J., 2019. Evaluation of atmospheric correction algorithms over spanish inland waters for sentinel-2 multi spectral imagery data. *Remote Sens. (Basel)* 11, 1–23. <https://doi.org/10.3390/rs11121469>.
- Qin, P., Simis, S.G.H., Tilstone, G.H., 2017. Radiometric validation of atmospheric correction for MERIS in the Baltic Sea based on continuous observations from ships and AERONET-OC. *Remote Sens. Environ.* 200, 263–280. <https://doi.org/10.1016/j.rse.2017.08.024>.
- Renosh, P.R., Doxaran, D., de Keukelaere, L., Gossn, J.I., 2020. Evaluation of atmospheric correction algorithms for sentinel-2-MSI and sentinel-3-OLCI in highly turbid estuarine waters. *Remote Sens. (Basel)* 12. <https://doi.org/10.3390/RS12081285>.
- Richter, R., Schläpfer, D., 2002. Geo-atmospheric processing of airborne imaging spectrometry data. Part 2: Atmospheric/topographic correction. *Int. J. Remote Sens.* 23, 2631–2649. <https://doi.org/10.1080/01431160110115834>.
- Schaeffer, B.A., Bailey, S.W., Conmy, R.N., Galvin, M., Ignatius, A.R., Johnston, J.M., Keith, D.J., Lunetta, R.S., Parmar, R., Stumpf, R.P., Urquhart, E.A., Werdell, P.J., Wolfe, K., 2018. Mobile device application for monitoring cyanobacteria harmful algal blooms using Sentinel-3 satellite Ocean and Land Colour Instruments. *Environ. Model. Softw.* 109, 93–103. <https://doi.org/10.1016/j.envsoft.2018.08.015>.
- Schroeder, T., Schaal, M., Lovell, J., Blondeau-Patissier, D., 2022. An ensemble neural network atmospheric correction for Sentinel-3 OLCI over coastal waters providing inherent model uncertainty estimation and sensor noise propagation. *Remote Sens. Environ.* 270. <https://doi.org/10.1016/j.rse.2021.112848> 112848.
- Siman, K., Kramar, D., Mackey, S., 2021. Social-ecological risk and vulnerability to flooding and erosion along the Ohio Lake Erie Shoreline. *Coast. Manag.* 50, 45–61. <https://doi.org/10.1080/08920753.2022.2006881>.
- Simis, S.G.H., Peters, S.W.M., Gons, H.J., 2005. Remote sensing of the cyanobacterial pigment phycocyanin in turbid inland water. *Limnol. Oceanogr.* 50, 237–245. <https://doi.org/10.4319/lo.2005.50.1.0237>.
- Simis, S.G.H., Ruiz-Verdú, A., Domínguez-Gómez, J.A., Peña-Martínez, R., Peters, S.W.M., Gons, H.J., 2007. Influence of phytoplankton pigment composition on remote sensing of cyanobacterial biomass. *Remote Sens. Environ.* 106, 414–427. <https://doi.org/10.1016/j.rse.2006.09.008>.
- Smith, B., Pahlevan, N., Schalles, J., Ruberg, S., Errera, R., Ma, R., Giardino, C., Bresciani, M., Barbosa, C., Moore, T., Fernandez, V., Alikas, K., Kangaro, K., 2021. A chlorophyll-a algorithm for Landsat-8 based on Mixture Density Networks. *Front. Remote Sens.* 1, 5. <https://doi.org/10.3389/frsen.2020.623678>.
- Soppa, M.A., Silva, B., Steinmetz, F., Keith, D., Scheffler, D., Bohn, N., Bracher, A., 2021. Assessment of polymer atmospheric correction algorithm for hyperspectral remote sensing imagery over coastal waters. *Sensors* 21, 1–16. <https://doi.org/10.3390/s21124125>.
- Spyrakos, E., O'Donnell, R., Hunter, P.D., Miller, C., Scott, M., Simis, S.G.H., Neil, C., Barbosa, C.A.F., Binding, C.E., Bradt, S., Bresciani, M., Dall'Olmo, G., Giardino, C., Gitelson, A.A., Kutser, T., Li, L., Matsushita, B., Martínez-Vicente, V., Matthews, M.W., Ogashawara, I., Ruiz-Verdú, A., Schalles, J.F., Tebbs, E., Zhang, Y., Tyler, A.N., 2018. Optical types of inland and coastal waters. *Limnol. Oceanogr.* 63, 846–870. <https://doi.org/10.1002/lno.10674>.

- Steinmetz, F., Deschamps, P.-Y., Ramon, D., 2011. Atmospheric correction in presence of sun glint: application to MERIS. *Opt. Express* 19, 9783. <https://doi.org/10.1364/oe.19.009783>.
- Theil, H., 1950. A rank-invariant method of linear and polynomial regression analysis. *Indag. Math.* 12, 173.
- Thuillier, G., Hersé, M., Simon, P.C., Labs, D., Mandel, H., Gillotay, D., 1998. Observation of the solar spectral irradiance from 200 nm to 870 nm during the ATLAS 1 and ATLAS 2 missions by the SOLSPEC spectrometer. *Metrologia* 35, 689. <https://doi.org/10.1088/0026-1394/35/4/79>.
- Tóth, V.Z., Ladányi, M., Jung, A., 2021. Adaptation and validation of a Sentinel-based chlorophyll-a retrieval software for the central European freshwater lake, Balaton. PFG – J. Photogrammetry, *Remote Sens. Geoinform. Sci.* 89, 335–344. <https://doi.org/10.1007/S41064-021-00160-1/FIGURES/8>.
- Vanhellemont, Q., 2019. Adaptation of the dark spectrum fitting atmospheric correction for aquatic applications of the Landsat and Sentinel-2 archives. *Remote Sens. Environ.* 225, 175–192. <https://doi.org/10.1016/J.RSE.2019.03.010>.
- Vanhellemont, Q., Ruddick, K., 2016. Acolite for Sentinel-2: Aquatic applications of MSI imagery. European Space Agency, (Special Publication) ESA SP SP-740, 9–13.
- Warren, M.A., Simis, S.G.H., Martinez-Vicente, V., Poser, K., Bresciani, M., Alikas, K., Spyarakos, E., Giardino, C., Ansper, A., 2019. Assessment of atmospheric correction algorithms for the Sentinel-2A MultiSpectral Imager over coastal and inland waters. *Remote Sens. Environ.* 225, 267–289. <https://doi.org/10.1016/J.RSE.2019.03.018>.
- Warren, M.A., Simis, S.G.H., Selmes, N., 2021. Complementary water quality observations from high and medium resolution Sentinel sensors by aligning chlorophyll-a and turbidity algorithms. *Remote Sens. Environ.* 265, <https://doi.org/10.1016/J.RSE.2021.112651> 112651.
- Watson, S.B., Miller, C., Arhonditsis, G., Boyer, G.L., Carmichael, W., Charlton, M.N., Confesor, R., Depew, D.C., Höök, T.O., Ludsin, S.A., Matisoff, G., McElmurry, S.P., Murray, M.W., Peter Richards, R., Rao, Y.R., Steffen, M.M., Wilhelm, S.W., 2016. The re-eutrophication of Lake Erie: Harmful algal blooms and hypoxia. *Harmful Algae* 56, 44–66. <https://doi.org/10.1016/j.hal.2016.04.010>.
- Windle, A.E., Evers-King, H., Loveday, B.R., Ondrusek, M., Silsbe, G.M., 2022. Evaluating atmospheric correction algorithms applied to OLCI Sentinel-3 data of Chesapeake Bay waters. *Remote Sensing* 2022, Vol. 14, Page 1881 14, 1881. <https://doi.org/10.3390/RS14081881>.
- Wynne, T.T., Stumpf, R.P., Tomlinson, M.C., Warner, R.A., Tester, P.A., Dyble, J., Fahnenstiel, G.L., 2008. Relating spectral shape to cyanobacterial blooms in the Laurentian Great Lakes. *Int. J. Remote Sens.* 29, 3665–3672. <https://doi.org/10.1080/01431160802007640>.
- Yuhua, R., Goetz, A., Boardman, J., 1992. Discrimination among semi-arid landscape endmembers using the spectral angle mapper (SAM) algorithm.
- Zibordi, G., Holben, B., Slutsker, I., Giles, D., D'alimonte, D., Mélin, F., Berthon, J.F., Vandemark, D., Feng, H., Schuster, G., Fabbri, B.E., Kaitala, S., Seppälä, J., 2009. AERONET-OC: A network for the validation of ocean color primary products. *J. Atmos. Ocean Technol.* 26, 1634–1651. <https://doi.org/10.1175/2009JTECH0654.1>.
- Zolfaghari, K., Pahlevan, N., Binding, C., Gurlin, D., Simis, S.G.H., Verdu, A.R., Li, L., Crawford, C.J., VanderWoude, A., Errera, R., Zastepa, A., Duguay, C.R., 2021. Impact of spectral resolution on quantifying cyanobacteria in lakes and reservoirs: A machine-learning assessment. *IEEE Trans. Geosci. Remote Sens.* 1–20. <https://doi.org/10.1109/TGRS.2021.3114635>.